Čizmar *et al. Cell Communication and Signaling* (2026) 24:524
https://doi.org/10.1186/s12964-026-03074-w

Cell Communication and Signaling

RESEARCH Open Access

IqgD is a Rac1-interacting IQGAP required for efficient growth of *Dictyostelium discoideum* on bacterial lawns

Anja Čizmar[1†], Darija Putar[1†], Marija Šimić[1], Jonas Scholz[2], Maja Marinović[1], Lucija Horvat[1], Mihaela Matovina[3], Igor Weber[1], Jan Faix[2] and Vedrana Filić[1*]

Abstract

Background Phagocytosis of surface-bound microbes is essential for host defence and environmental feeding, yet the mechanism by which macrophages remove surface-bound particles has only recently been described. This process involves the formation of an F-actin-rich, force-bearing ring around the surface-attached particle. Here, we identify the IQGAP-related protein IqgD from the professional phagocyte *Dictyostelium discoideum* as a key regulator of mechanically demanding phagocytosis. IQGAPs are large multidomain scaffold proteins that interact with Rho family GTPases and F-actin. IqgD contains a calponin homology domain (CHD), a GAP-related domain (GRD), a RasGAP C-terminal (RGCT), and an extreme C-terminal (CT) domain.

Methods In this study, we used biochemical and imaging approaches with full-length and truncated protein variants to investigate whether IqgD interacts with *D. discoideum* Rho GTPases and F-actin. We also performed comprehensive phenotypic characterisation of IqgD-deficient cells to determine the cellular function of IqgD.

Results We show that the CHD is essential for F-actin binding and cortical localisation, while the GRD and CT domains mediate interactions with Rac1 GTPases and the actin-bundling proteins cortexillins. Moreover, similar to mammalian IQGAPs, IqgD maintains Rac1 in its active conformation. Although IqgD is enriched in macropinocytic and phagocytic cups, it is not required for fluid uptake or internalisation of bacteria from suspension. However, loss of IqgD markedly reduces growth on bacterial lawns and strongly impairs uptake of surface-attached microbeads and yeast particles. Furthermore, IqgD localises to F-actin-rich ring-like structures that form around surface-bound particles at the basal cell surface.

Conclusions IqgD is not required for all forms of macroendocytosis; rather, it is specifically required for mechanically demanding phagocytosis. This includes the formation of enlarged phagocytic cups during phagocytosis of yeast particles or the generation of greater force, as in phagocytosis of surface-bound particles and bacteria within bacterial lawns. Similar to phagocytosis of surface-attached particles in mammalian macrophages, *D. discoideum* also forms an F-actin-rich ring around the particle at the cell base, suggesting that force-driven particle detachment

[†]Anja Čizmar and Darija Putar contributed equally to this work.

*Correspondence:
Vedrana Filić
vedrana.filic@irb.hr

Full list of author information is available at the end of the article

© The Author(s) 2026. **Open Access** This article is licensed under a Creative Commons Attribution-NonCommercial-NoDerivatives 4.0 International License, which permits any non-commercial use, sharing, distribution and reproduction in any medium or format, as long as you give appropriate credit to the original author(s) and the source, provide a link to the Creative Commons licence, and indicate if you modified the licensed material. You do not have permission under this licence to share adapted material derived from this article or parts of it. The images or other third party material in this article are included in the article's Creative Commons licence, unless indicated otherwise in a credit line to the material. If material is not included in the article's Creative Commons licence and your intended use is not permitted by statutory regulation or exceeds the permitted use, you will need to obtain permission directly from the copyright holder. To view a copy of this licence, visit http://creativecommons.org/licenses/by-nc-nd/4.0/.

and internalisation may be an evolutionarily conserved mode of substrate-dependent phagocytosis. Our findings provide mechanistic insight linking IqgD with Rac1, cortexillins, and F-actin in the regulation of demanding forms of phagocytosis.

Keywords IQGAP, IqgD, Rac1, Cortexillin, Phagocytosis, *Dictyostelium*

Background

IQ motif-containing GTPase-activating proteins (IQGAPs) constitute an evolutionarily conserved protein family in eukaryotes. Most vertebrates express three isoforms with similar domain architecture: an N-terminal calponin homology domain (CHD), followed by a coiled-coil repeat region (CC), a tryptophan-containing proline-rich motif-binding region (WW), an IQ domain containing several IQ motifs, a GTPase-activating protein (GAP)-related domain (GRD), a RasGAP C-terminal (RGCT) domain, and an extreme C-terminal (CT) domain (Fig. 1) [1, 2]. These multidomain proteins act as scaffolds modulating various signalling pathways by bringing their components into close proximity. For example, the best-studied IQGAP, human IQGAP1, promotes the mitogen-activated protein kinase (MAPK) signalling pathway by directly binding B-Raf, C-Raf, MEK1/2, and ERK1/2 [3–6]. IQGAP1 also facilitates PI3K/Akt signalling by binding three phosphoinositide kinases that sequentially generate phosphatidylinositol 3,4,5-trisphosphate ($PI(3,4,5)P_3$) from phosphatidylinositol, as well as Akt and PDK1, which are recruited to $PI(3,4,5)P_3$ [7]. IQGAPs interact with various cell surface receptors and serve as scaffolds for their signalling components, modulating their activation and signalling [8]. Last but not least, IQGAPs are important regulators of the actin cytoskeleton [9].

Although IQGAPs harbour the GRD, which is structurally very similar to the RasGAP domain, their catalytic activity to promote GTP hydrolysis on Ras GTPases appears to have been lost early in evolution due to mutations in key amino acid residues [10–12]. Furthermore, IQGAPs do not bind the canonical GTPases of the Ras family [13]. Instead, they interact with the Rho family GTPases, Cdc42 and Rac1, and stabilise their active forms [14–18]. Overexpression and silencing of IQGAP1 lead to increased and decreased levels of active Cdc42, respectively [19–21]. Binding of Cdc42 to IQGAP1 requires the GRD, but additional regions, particularly in the C-terminal part of IQGAP1, contribute to GTPase binding [15, 19–21]. More recently, a multistep binding mechanism has been proposed [22, 23]. The authors suggested that RGCT is the central domain that initially associates with the switch regions of GTP-loaded Cdc42 and Rac1, while the GRD subsequently mediates low-affinity, partially nucleotide-dependent binding outside the switch regions. The CT domain binds with extremely low affinity outside the switch regions and most likely stabilises the interaction between IQGAP1 and Cdc42.

IQGAPs influence the activity of Rho family GTPases by maintaining their activated state, but also act as their effectors [24]. IQGAPs bind microfilaments directly via the CHD and cross-link them into loosely organised bundles [25–27]. This activity depends on their oligomerisation, which is enhanced by active Cdc42 [26]. Furthermore, IQGAP1 directly influences actin dynamics as a barbed end capper that transiently arrests filament growth and prevents depolymerisation from the barbed end [27, 28]. In addition, IQGAP1 interacts with N-WASP, although there are conflicting data on whether it activates N-WASP and thereby stimulates Arp2/3-mediated nucleation of branched actin filaments [28–31]. Recent work has shown that IQGAP1 regulates filament growth by displacing barbed end binding proteins such as formin Dia1 or the complex of Dia1 and the capping factor CP, which determines the polymerisation fate of a single filament [32, 33]. Based on these activities, IQGAPs are involved in fundamental cellular processes, including cell migration, cytokinesis, and endocytosis [34].

The protist *Dictyostelium discoideum* expresses four proteins with adjacent GRD, RGCT, and CT domains, which are present in all IQGAPs: DGAP1, GAPA, IqgC, and IqgD [35]. However, DGAP1, GAPA, and IqgC lack the N-terminal domains found in IQGAPs from higher eukaryotes and therefore cannot interact directly with actin filaments. Notably, DGAP1 and GAPA interact with actin-binding proteins, the cortexillins, which are unique to Amoebozoa, and bridge the gap between these truncated IQGAPs and F-actin [36]. The association of DGAP1 or GAPA with a cortexillin dimer requires the binding of active Rac1 to DGAP1 or GAPA. The Rho family of GTPases in *D. discoideum* comprises 20 Rac GTPases, six of which belong to the Rac subfamily (Rac1A, Rac1B, Rac1C, RacF1, RacF2, and RacB) [37, 38]. Rac1A, Rac1B, and Rac1C are *D. discoideum* orthologues of human Rac1. They share more than 90% amino acid sequence identity and have an identical effector-binding domain. The aforementioned tetrameric complex of active Rac1, DGAP1 or GAPA, and a cortexillin dimer forms in the retractive cortex of interphase cells and in the cleavage furrow of dividing cells, and is important for efficient migration and cytokinesis [36, 39, 40]. Functional characterisation of IqgC revealed that, in contrast to DGAP1 and GAPA, IqgC exhibits RasGAP activity and is involved

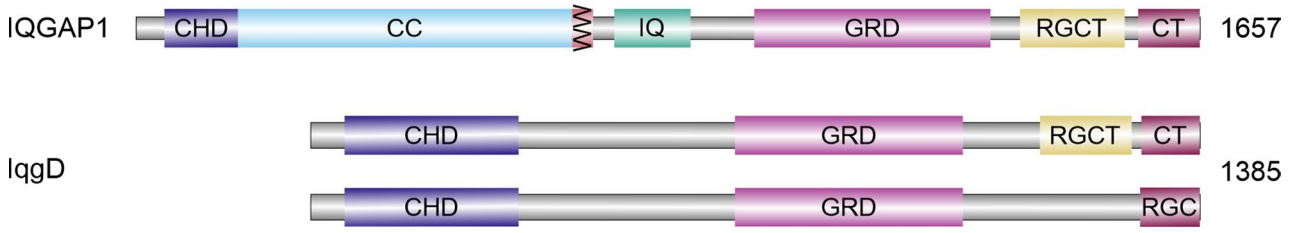


Fig. 1 Domain architecture of *D. discoideum* IqgD compared with human IQGAP1. IqgD contains a calponin homology domain (CHD), a GTPase-activating protein (GAP)-related domain (GRD), a RasGAP C-terminal (RGCT) domain, and an extreme C-terminal (CT) domain. However, it lacks the coiled-coil repeat region (CC), the tryptophan-containing region (WW), and the IQ domain present in human IQGAP1. The numbers on the right indicate the number of amino acid residues in each protein. The boundaries of the GRD, RGCT, and CT domains are shown according to the recently published computationally predicted 3D structure of IqgD obtained using the biomolecular structure prediction tool AlphaFold 3 (*upper schematic of IqgD*). However, the bioinformatics database InterPro, which we used to identify domains in IqgD in this study, recognised the CHD, GRD, and an RGC domain-like module (RGC) at the very C-terminus, whereas the RGCT domain was not predicted (*lower schematic of IqgD*). The RGC corresponds to the CT domain in the upper schematic

in the regulation of macroendocytosis [41, 42]. This is consistent with phylogenetic analysis, which places IqgC closer to the Gap1 family of RasGAPs from fungi than to IQGAPs from *Dictyostelium* [12, 43]. IqgD is the only IQGAP-related protein in *D. discoideum* that contains an N-terminal CHD and is significantly larger than DGAP1, GAPA, and IqgC. Interestingly, the bioinformatics tool InterProScan recognises the CHD, GRD, and an RGC domain-like module at the very C-terminus, whereas the RGCT domain, located further upstream in human IQGAP1 and *Dictyostelium* DGAP1, GAPA, and IqgC, is not predicted from the primary sequence in IqgD (Fig. 1, *lower schematic of IqgD*) [44]. However, while finalising this manuscript, we performed computational analysis of the 3D structure of IqgD using the biomolecular structure prediction tool AlphaFold 3, which suggests that IqgD, like the aforementioned IQGAPs, also contains the GRD, RGCT, and CT domain triad (Fig. 1, *upper schematic of IqgD*) [35, 45]. From both predictions, it is evident that the RGC domain-like module corresponds to the CT domain. Therefore, to adhere to the nomenclature used in the recent literature [2, 23, 35], we refer to this domain throughout the text as the CT. Notably, the experimental design of truncated IqgD proteins was based on the awareness of the existence of CHD, GRD, and RGC-like/CT domains at the time. Here, we show that IqgD binds to Rac1 GTPases, F-actin, and cortexillins. As in mammalian IQGAPs, IqgD binding to F-actin is mediated by the CHD, while its interaction with Rac1 requires the GRD and CT domains. We also show that IqgD maintains Rac1 GTPase in an active state and that Rac1-bound IqgD cannot interact with cortexillin. Based on these findings and its localisation to cortical structures, with strong enrichment in macropinocytic and phagocytic cups, we hypothesised that IqgD is required for efficient macroendocytosis. Surprisingly, comprehensive phenotypic characterisation of cells lacking IqgD showed that it is dispensable for the uptake of fluid and suspended bacteria. However, IqgD depletion leads to dramatically reduced growth on bacterial lawns and significantly reduced cell-substrate adhesion. Additionally, IqgD-deficient cells ingest surface-immobilised microbeads less efficiently than wild-type cells, and their uptake of yeast particles is strikingly diminished. Interestingly, IqgD accumulates in F-actin-rich circular structures at the cell bottom that form around surface-bound particles. An analogous F-actin-containing ring structure, important for phagocytosis of surface-attached microbes, was recently described in mammalian macrophages [46]. Together, these data provide evidence that IqgD is specifically required for mechanically demanding phagocytosis, such as phagocytosis of large particles or surface-attached bacteria, which is the principal feeding mechanism in this unicellular organism in its natural environment. Furthermore, this study offers additional insight into the molecular basis of phagocytosis of surface-bound particles in general, thereby contributing to a broader understanding of this process, which is fundamental to innate immunity.

Results

IqgD localises to F-actin-rich structures

To investigate the role of IqgD during growth, we examined the subcellular localisation of fluorescently labelled IqgD during random movement, phagocytosis, and cytokinesis in vegetative wild-type cells (Fig. 2). IqgD was fused at both the N- and C-termini to yellow fluorescent protein (YFP), and both fusion proteins localised throughout the cell cortex and were strongly enriched in macropinocytic and phagocytic cups (Fig. 2A-C, Videos 1–3, Fig. 3A, and Fig. S1). While IqgD appeared evenly distributed on developing macropinosomes, it was markedly enriched at the base of forming phagocytic cups. As phagocytosis progressed, IqgD shifted from the base to distal regions of the cup and accumulated strongly at the site of cup closure. During cytokinesis, IqgD was approximately evenly distributed throughout the cortex (Fig. 2D).

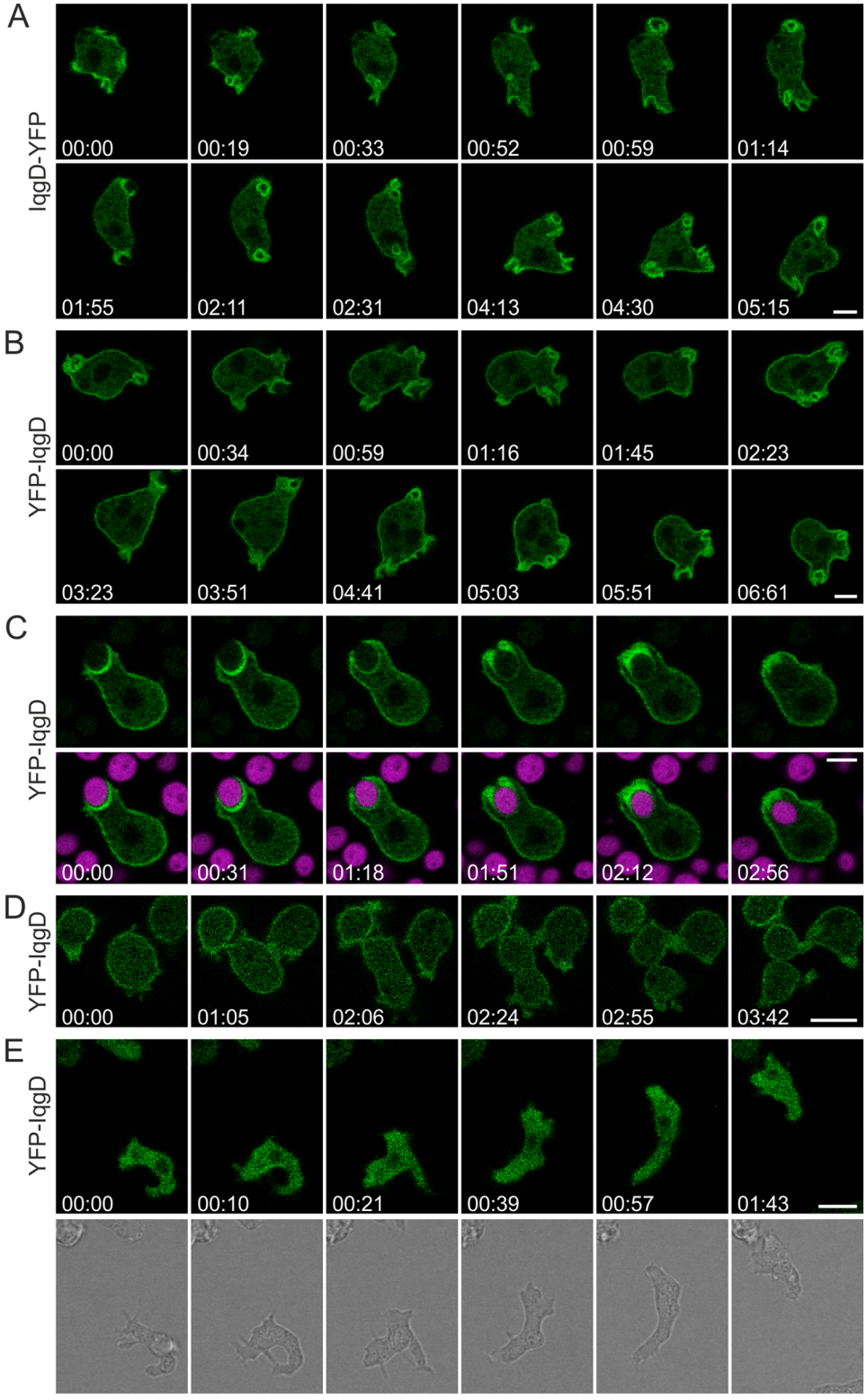


Fig. 2 IqgD localises across the entire cortex in vegetative cells, with strong enrichment at macropinosomes and phagosomes. Image sequences show growth-phase wild-type cells extrachromosomally expressing (**A**) IqgD-YFP and (**B**) YFP-IqgD during random movement and macropinocytosis, (**C**) YFP-IqgD during phagocytosis of TRITC-labelled yeast (*magenta*), and (**D**) cytokinesis. **E** YFP-IqgD is cytosolic in migrating starved cells. Time is shown in min:sec format. Scale bars: (**A**-**C**) 5 µm; (**D**, **E**) 10 µm. **A**-**C** correspond to Videos 1–3

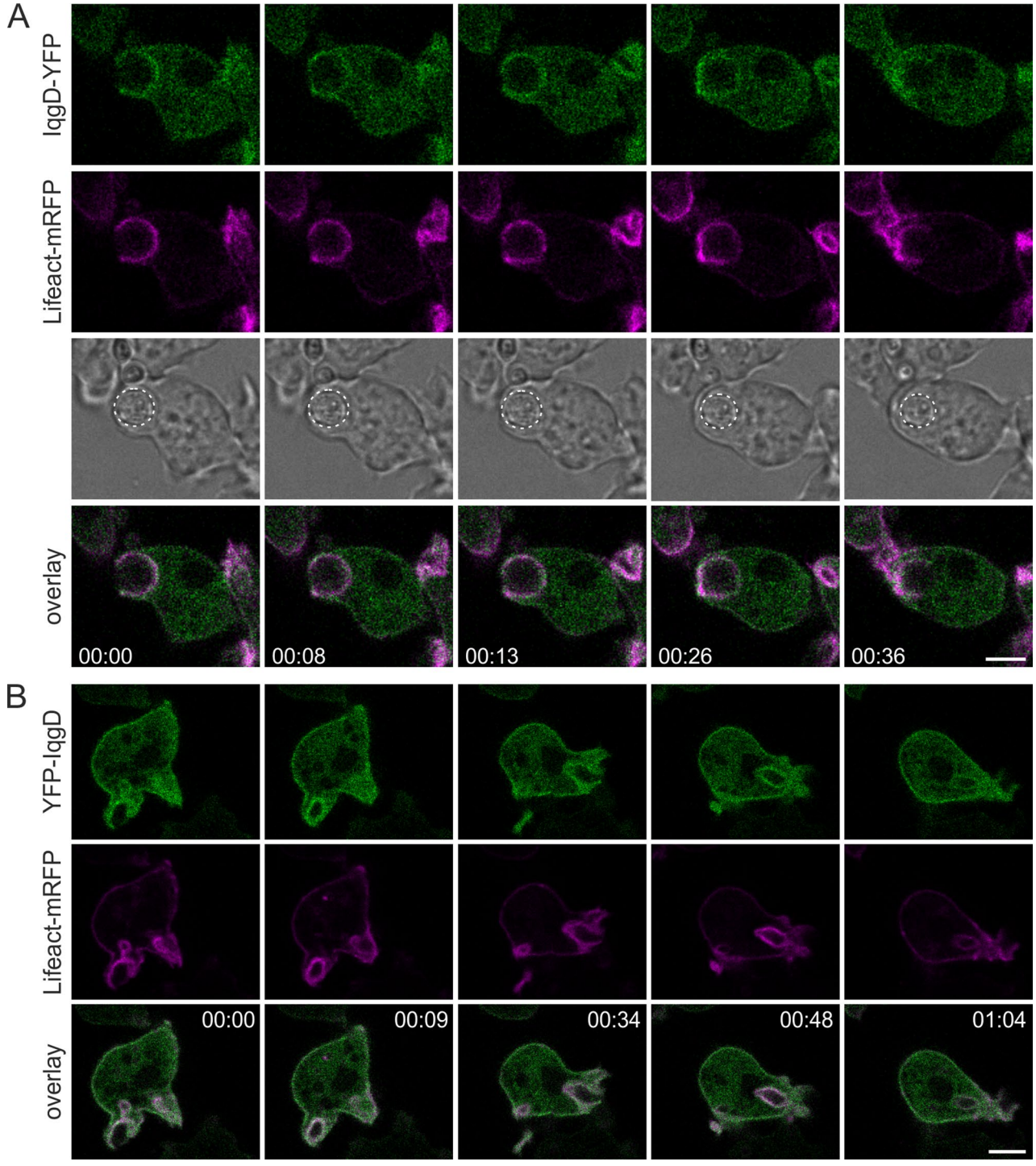


Fig. 3 IqgD is colocalised with the F-actin marker Lifeact-mRFP during random movement, macropinocytosis, and phagocytosis. **A** Image sequence of a growth-phase wild-type cell ectopically expressing IqgD-YFP and Lifeact-mRFP during phagocytosis of a yeast particle. Dashes in the transmission channel outline the yeast particle. **B** Image sequence of a growth-phase wild-type cell ectopically expressing YFP-IqgD and Lifeact-mRFP during random movement and macropinocytosis. Time is shown in min: sec format. Scale bars: 5 µm

The localisation of IqgD during growth closely resembled the distribution of F-actin in vegetative cells. Consistent with this, co-expression of IqgD-YFP (Fig. 3A) or YFP-IqgD (Fig. 3B) with the F-actin marker Lifeact-mRFP [47] revealed almost complete colocalisation at the cell cortex and within macropinocytic and phagocytic cups. As YFP-IqgD labelled the cell cortex more strongly than IqgD-YFP, all subsequent localisation experiments were

performed using the N-terminally tagged construct. To examine whether IqgD localises to the leading edge of migrating cells, we analysed its distribution in starved cells displaying prominent pseudopods. We found that IqgD was not enriched at the leading edge; instead, it was more or less homogeneously cytosolic (Fig. 2E).

The axenic strain AX2-214 harbours two copies of the *iqgD* gene

To investigate the cellular function of IqgD, we aimed to generate IqgD-deficient cells by inactivating *iqgD* using homologous recombination. Although a unique recombination event at the target locus ($iqgD^{L1}$) was confirmed by PCR, Southern blotting, and immunoblotting with a polyclonal anti-IqgD antibody raised against the N-terminal fragment of IqgD (Fig. S2A), we discovered a second copy of the gene (designated $iqgD^{L2}$) in the *D. discoideum* genome (Fig. S2B). However, this second locus appears to be poorly expressed, as evidenced by strikingly reduced transcript levels in $iqgD^{L1-}$ cells (Fig. S2C). According to the sequenced genome of the AX4 strain, the *iqgD* gene is located on chromosome 2 (http://dictybase.org/gene/DDB_G0275731) at a position not encompassed by the 750 kb inverted duplication present in this strain [48, 49]. Although the AX2-214 strain we used does not contain this duplication, it does have certain duplications on chromosome 2 [50]. However, based on their chromosomal locations, these do not explain the presence of another *iqgD* locus. To determine whether the presence of an alternative *iqgD* locus is intrinsic to strain AX2-214 or a result of cell propagation in our laboratory, we obtained a vial of AX2-214 spores stored in 1992. We repeated the homologous recombination and confirmed the inactivation of $iqgD^{L1}$ by PCR (Fig. S2D) and western blot (Fig. S2A). However, PCR with primers specific for $iqgD^{L2}$ confirmed the presence of the second locus (Fig. S2E). Sequencing the first 2.47 kb of $iqgD^{L2}$ using genomic DNA from cells with inactivated $iqgD^{L1}$ ($iqgD^{L1-}$) revealed that the sequence is identical to that of $iqgD^{L1}$, except that all introns are absent. Therefore, $iqgD^{L2}$ appears to be a weakly active retrogene (Fig. S2F). To formally exclude residual expression from the second locus, we excised the bsr resistance cassette from $iqgD^{L1-}$ cells by transient expression of Cre recombinase and subsequently inactivated $iqgD^{L2}$ by homologous recombination. Successful inactivation of $iqgD^{L2}$ was confirmed by PCR and sequencing (Fig. S2G).

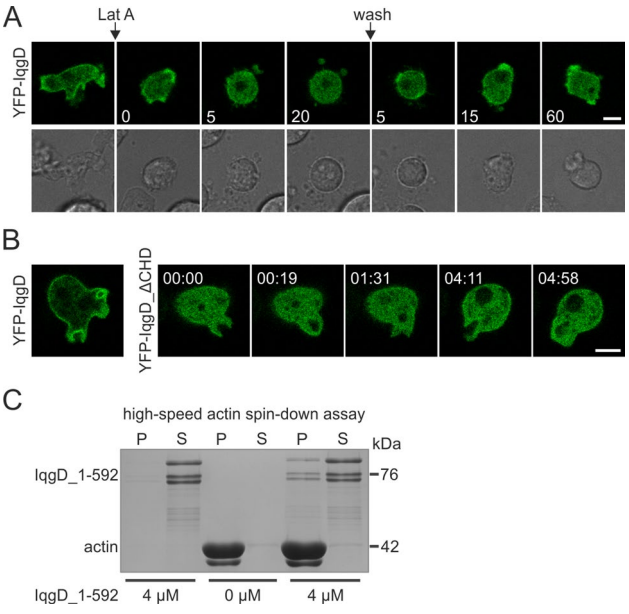


Fig. 4 Cortical localisation of IqgD requires interaction of the CHD with an intact cortical F-actin network. **A** Wild-type cell expressing YFP-IqgD before, during, and after treatment with 5 μM Latrunculin A. The numbers to the right of the *Lat A* label indicate minutes after addition of latrunculin. The numbers to the right of the *wash* label indicate minutes after washing the cells with fresh medium. **B** Image sequence of a representative vegetative IqgD-deficient cell expressing YFP-IqgD_ΔCHD. **C** The Coomassie Brilliant Blue (CBB)-stained PAG of the high-speed actin spin-down assay shows that IqgD_1-592 produced in insect cells co-sediments with F-actin. *P* and *S* indicate the pellet and supernatant, respectively. In (**B**), time is shown in min: sec format. Scale bars: 5 μm. **B** corresponds to Video 4

IqgD interacts with F-actin via its CHD

To investigate whether IqgD interacts with F-actin, we performed an actin co-sedimentation assay using bacterially purified protein. Because full-length IqgD was poorly expressed in bacterial cells, we purified an N-terminal fragment (amino acids 1-575) containing the CHD. The actin co-sedimentation assay with this fragment showed no detectable interaction with F-actin (Fig. S3A). We then performed co-immunoprecipitation with an anti-IqgD antibody raised against the same N-terminal fragment to test whether actin binds to endogenous IqgD. However, actin bound substantially to the protein A-Sepharose beads even in the absence of the anti-IqgD antibody, making this method unsuitable for detecting IqgD-actin interaction (Fig. S3B). Therefore, we used indirect approaches to assess whether IqgD associates with F-actin. First, we monitored the localisation of YFP-IqgD during disruption of the actin cytoskeleton with Latrunculin A (Fig. 4A). Shortly after Latrunculin A addition, the cells rounded up, and within five minutes YFP-IqgD largely detached from the cortex. After 20 min, the signal became completely cytosolic. After washing out the drug, YFP-IqgD reappeared at the cell cortex. We then examined the localisation of an IqgD variant lacking the CHD, IqgD_ΔCHD (Fig. 4B and Video 4). This truncated protein was diffusely cytosolic and failed to accumulate in macropinocytic cups. These experiments showed that IqgD localisation to F-actin-rich structures requires an intact cortical actin network and depends

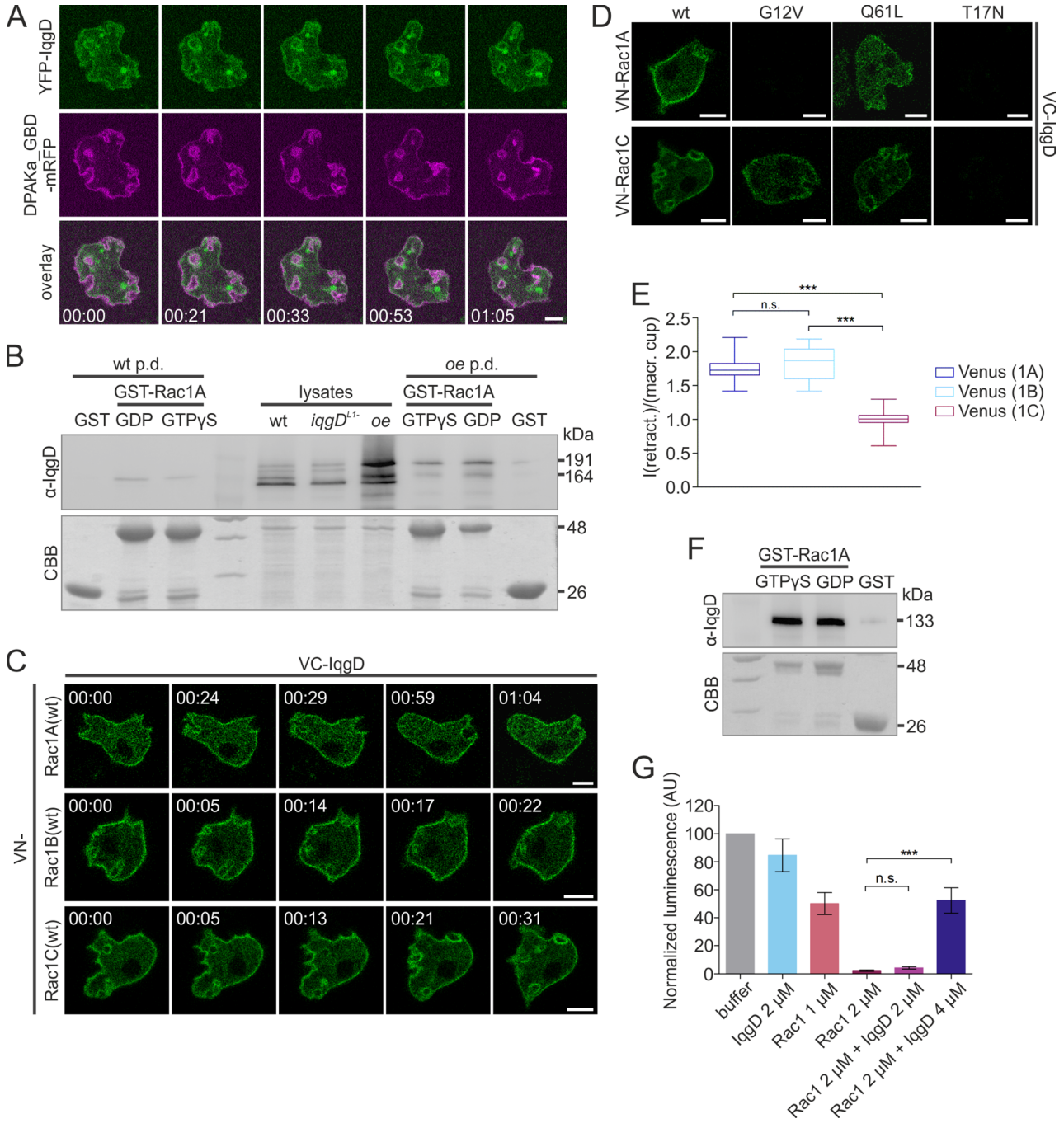


Fig. 5 (See legend on next page.)

on its CHD. Prompted by these results, we repeated the actin co-sedimentation assay with an N-terminal fragment (amino acids 1-592) of IqgD produced in insect cells. Using this protein produced in eukaryotic cells, we detected direct binding to F-actin in the co-sedimentation assay (Fig. 4C). Additionally, we compared F-actin distribution in cells with different IqgD levels. Immunofluorescence with an anti-actin antibody showed similar actin distribution in wild-type, IqgD-deficient, and IqgD-overexpressing cells (Fig. S3C). Quantification of the F- to G-actin ratio showed no difference between wild-type and IqgD-deficient cells (Fig. S3D). However, the F-actin level was significantly increased in IqgD-overexpressing cells.

IqgD interacts with active Rac1 GTPases in living cells

The localisation of IqgD to macropinosomes and phagosomes suggests its involvement in macroendocytosis.

(See figure on previous page.)

Fig. 5 IqgD interacts with active Rac1 GTPases in living cells and maintains their active state. **A** Image sequence of a wild-type vegetative cell expressing YFP-IqgD and the probe for active Rac1 GTPases, DPAKa_GBD-mRFP. **B** Anti-IqgD blot of GST-Rac1A pull-down with lysates of wild-type cells (*wt p.d.*) and wild-type cells expressing YFP-IqgD (*oe p.d.*) shows that both endogenous IqgD (164 kDa) and exogenous YFP-IqgD (191 kDa) interact with GTPγS- and GDP-loaded Rac1A. The GST pull-down was performed as a negative control. Lysate from *iqgD*$^{L1-}$ cells was loaded in the centre of the membrane to facilitate recognition of a specific band. See also Fig. S2A. **C** Image sequences of vegetative *iqgD*$^{L1-}$ cells expressing VC-IqgD with VN-Rac1A(wt) (*upper panel*), VN-Rac1B(wt) (*middle panel*), or VN-Rac1C(wt) (*lower panel*). **D** Images of *iqgD*$^{L1-}$ cells expressing VC-IqgD with VN-Rac1A(wt/G12V/Q61L/T17N) (*upper panel*) or VN-Rac1C(wt/G12V/Q61L/T17N) (*lower panel*). Cells with the strongest observed signals are shown. **E** The ratios of Venus intensity in the retracting cortical region, *I(retract.)*, and at the base of the macropinocytic cup, *I(macr. cup)*, were determined for cells shown in Fig. S5A – C and were as follows: 1.75 ± 0.21 for VC-IqgD and VN-Rac1A; 1.84 ± 0.26 for VC-IqgD and VN-Rac1B; and 0.99 ± 0.18 for VC-IqgD and VN-Rac1C (mean ± SD). **F** Anti-IqgD blot of GST-Rac1A pull-down with IqgD_311–1385 purified from insect cells confirms direct binding of IqgD to Rac1A. The GST pull-down was performed as a negative control. **G** The results of the GAP assay show that IqgD_311–1385 added in double concentration to human Rac1 reduces its intrinsic GTPase activity (compare *Rac1 2 μM* with *Rac1 2 μM + IqgD 4 μM*). An equimolar concentration of IqgD_311–1385 was not sufficient to significantly increase luminescence, i.e. to reduce GTP hydrolysis by Rac1. Data are from 3 independent experiments (mean ± SD). In (**A**) and (**C**), time is shown in min: sec format. Scale bars: 5 μm. In (**B**) and (**F**), CBB-stained PAGs are shown beneath the blots. Statistical analyses in (**E**) and (**G**) were performed using one-way ANOVA followed by Tukey's multiple comparison test. The significance level was set at 5%. n.s. – not significant, *** $P < 0.001$

Additionally, IqgD contains a GRD, which mediates interactions between IQGAPs and Ras superfamily GTPases [29]. Therefore, we tested the interaction of IqgD with Ras and Rho family GTPases known to be involved in macroendocytosis. A yeast two-hybrid assay with full-length IqgD showed weak interactions with the GTPases Rac1A and Rac1C (Fig. S4A), whereas the assay using only the GRD of IqgD detected interactions with the constitutively active forms of all three Rac1 GTPases (Fig. S4B). We then co-expressed YFP-IqgD and a probe for active Rac1 GTPases in *D. discoideum* cells and showed that IqgD largely colocalises with active Rac1 [51] (Fig. 5A). Next, we performed a GST-Rac1A pull-down assay with lysates of wild-type and IqgD-overexpressing cells and found that both endogenous and extrachromosomally expressed IqgD bind to both GTPγS- and GDP-loaded Rac1A (Fig. 5B). The binding was even somewhat stronger to the GDP-loaded GTPase. This was corroborated in an independent GST-Rac1A pull-down using constitutively active and constitutively inactive Rac1A mutants (Fig. S4C). To evaluate direct interactions between IqgD and Rac1 GTPases in live *D. discoideum* cells, we used the bimolecular fluorescence complementation (BiFC) assay. *IqgD* knockout (*iqgD*$^{L1-}$) cells were transfected with an expression vector allowing simultaneous expression of IqgD fused at its N-terminus to the C-terminal part of the fluorescent protein Venus (VC-IqgD) and the respective Rac1 GTPase fused at its N-terminus to the N-terminal part of Venus (VN-Rac1). Complementation of the Venus protein due to interaction between IqgD and the tested GTPase resulted in a strong fluorescent signal for the wild-type forms of all three Rac1 GTPases (Fig. 5C). To assess the relevance of the nucleotide status of the interacting GTPase, we co-expressed VC-IqgD with VN-Rac1A/1C GTPases as mutant variants: two constitutively active (G12V and Q61L) and one constitutively inactive (T17N) variant. A fluorescent signal was detected only with the constitutively active Rac1 variants (Fig. 5D). However, the signal intensity was markedly weaker compared to the wild-type GTPases and was observed in significantly fewer cells (18% and 38% for wild-type Rac1A and Rac1C respectively vs. 2.5–3.5% for mutants with BiFC signal). The strong cortical BiFC signal obtained with wild-type GTPases indicated that GTPase cycling is required and suggested that interactions between IqgD and Rac1 GTPases occur throughout the cell cortex, consistent with the localisation of YFP-IqgD. However, closer inspection revealed subtle differences in the distribution of YFP-IqgD and the BiFC signals. Specifically, YFP-IqgD was enriched in the macropinocytic and phagocytic cups, whereas the Venus signals, particularly those from the interaction of wild-type Rac1A and Rac1B with IqgD, were stronger in the retractive regions of the cell cortex and weaker at the macropinocytic cups (compare Fig. 2B and C with *the upper and middle panels* in Fig. 5C). In contrast, the Venus signal resulting from the interaction of Rac1C with IqgD appeared equally strong at the macropinosomes and in the remaining cortical regions (Fig. 5C, *lower panel*). To verify this observation, we expressed all three VN-VC protein pairs together with the probe for active Ras as a marker for macropinocytic cups and measured the Venus signal intensity at the cup base and in the retractive region of the cell cortex (Fig. S5A-C). The BiFC signals indicating interactions between IqgD and Rac1A or Rac1B were about 80% stronger at the retractive regions of the cell cortex than at the base of the macropinocytic cups (Fig. 5E). In contrast, the signal from the interaction between IqgD and Rac1C showed no preference for any particular cortical region.

Finally, after establishing that IqgD interacts with active Rac1 GTPases in living cells, we examined whether it acts as a GAP for Rac1. To this end, we attempted to purify several truncated IqgD variants containing the GRD with or without the CT domain from *E. coli*, but were unable to obtain a soluble protein. Therefore, we again produced the protein from insect cells and successfully obtained IqgD_311–1385, the truncated variant containing the GRD, RGCT and CT domains. To confirm that the protein is biologically functional, we repeated the

GST-Rac1A pull-down assay with IqgD_311–1385 and showed that it binds strongly to both GTPγS- and GDP-bound forms of Rac1A with similar affinities (Fig. 5F). We then measured the GTPase activity of human Rac1 in the presence and absence of IqgD_311–1385 and showed that IqgD has no GAP activity towards Rac1 (Fig. 5G). Moreover, similar to its mammalian counterparts, IqgD inhibited the intrinsic GTPase activity of Rac1, thus stabilising its active state. Since the Rac1 GTPases of *D. discoideum* are more than 80% identical to human Rac1 and share the same effector binding domain, we argue that it is valid to use human Rac1 as a proxy for *D. discoideum* Rac1 GTPases in a GAP assay. Supporting this, it has been demonstrated that both human Rac1 and *D. discoideum* Rac1A bind with high affinity to DGAP1, another member of the IQGAP family in *D. discoideum* [52].

IqgD binding to cortexillins and Rac1 is mutually exclusive

A recent study showed that the GRD, RGCT, and CT domains of human IQGAP1 are involved in binding Cdc42 and Rac1 [22]. We investigated the importance of the GRD and CT domains of IqgD in binding *D. discoideum* Rac1 GTPases. We chose Rac1C for this analysis because the BiFC signal indicating interaction between IqgD and Rac1C was equally strong at both macropinocytic cups and in the remaining non-cup cortical regions (Fig. S5C and Fig. 5E). We transfected *iqgD*$^{L1-}$ cells with three additional BiFC constructs to express VC fused with either IqgD lacking the GRD, IqgD lacking the CT, or the GRD alone, together with VN-Rac1C(wt). In contrast to cells transfected with the BiFC construct encoding full-length IqgD (VC-IqgD_FL), which displayed cortical fluorescence in many cells, cells expressing IqgD without the GRD (VC-IqgD_ΔGRD) or the GRD alone (VC-IqgD_GRD) showed only weak Venus fluorescence in a small fraction of cells (38% for IqgD_FL vs. 3.4% and 1.6% for IqgD_ΔGRD and IqgD_GRD respectively) (Fig. 6A). No fluorescence was observed in cells expressing IqgD without the CT domain (VC-IqgD_ΔCT). These results suggest that both the CT and GRD contribute to Rac1 binding.

Next, we examined the localisation of truncated IqgD variants lacking either the GRD or the CT domain. Interestingly, deletion of either domain resulted in a clear separation of IqgD localisation between macropinocytic cups and the remaining cortex (Fig. 6B, Videos 5 and 6). To quantify this effect, we compared fluorescence intensity profiles along the cell cortex in cells of similar morphology containing two macropinocytic cups. As expected, YFP-IqgD_FL was enriched at macropinocytic cups, where the signal intensity was almost twice as high as in the rest of the cortex (Fig. 6C). IqgD_ΔGRD showed similar enrichment at macropinocytic cups, but was almost absent from non-cup cortical regions. Conversely, YFP-IqgD_ΔCT was excluded from macropinocytic cups, while its signal intensity in the remaining cortex was comparable to that of the full-length protein. These findings strongly suggest that the CT domain is required for recruiting IqgD to macropinocytic cups, whereas the GRD is important for its localisation to the rest of the cortex. We previously showed that Rac1 GTPases play a dual role in regulating the actin cytoskeleton in *D. discoideum* [39]. At the protrusive area, Rac1-GTP promotes dendritic actin nucleation by activating WASP family proteins upstream of the Arp2/3 complex [38]. In the retractive regions, Rac1-GTP promotes the formation of a tetrameric complex consisting of DGAP1 or GAPA and a dimer of the actin-binding proteins, the cortexillins, which bundle actin filaments [36, 53]. The localisation of IqgD_ΔGRD closely resembles that of a DPAKa_GBD probe specific for active Rac1 GTPases in protrusions, whereas IqgD_ΔCT adopts the same localisation in the retractive cortex as the Rac1 interactor DGAP1 [39]. Therefore, we investigated whether IqgD, similar to DGAP1 and GAPA, also interacts with the cortexillins. In a co-immunoprecipitation assay using an anti-IqgD antibody, both cortexillin I (CI) and II (CII) co-precipitated with endogenous IqgD (Fig. 6D). To test whether the binding is direct, we again performed a BiFC assay. *IqgD*$^{L1-}$ cells were transfected with VN-CI or VN-CII together with either VC-IqgD_FL, VC-IqgD_ΔGRD, or VC-IqgD_ΔCT. We observed a strong fluorescent signal in the retractive cortical regions of cells expressing either cortexillin with VC-IqgD_FL (Fig. 6E). However, in cells expressing truncated IqgD variants, no fluorescence was detected, suggesting that both the GRD and CT domains are required for binding to the cortexillins. Previously, it was shown that binding of DGAP1 or GAPA to the cortexillin dimer requires the association of active Rac1A with the IQGAP-related protein [36]. Since IqgD binds directly to Rac1A (Fig. 5C and F) as well as to CI and CII (Fig. 6E), we wondered whether IqgD might also participate in the formation of a tetrameric complex with Rac1 and the cortexillin dimer. To test this, we bound IqgD_311–1385 to GST-Rac1A as shown in Fig. 5F and added lysate of *dgap1*$^{-}$*/gapA*$^{-}$ cells to such immobilised IqgD. However, we did not detect CI or CII in the complex with Rac1-bound IqgD (Fig. 6F). This is consistent with previous findings showing that cortexillins cannot be detected in a GST-Rac1A pull-down using lysates from *dgap1*$^{-}$*/gapA*$^{-}$ cells [52]. To confirm that truncated IqgD_311–1385 can interact with the cortexillins, we performed a BiFC assay. Fluorescence was detected in cells co-expressing VC-IqgD_311–1385 and VN-CI or VN-CII (Fig. 6E), although the signal was weaker compared to full-length IqgD, probably because IqgD associates less efficiently with cortexillins in the absence of its CHD domain.

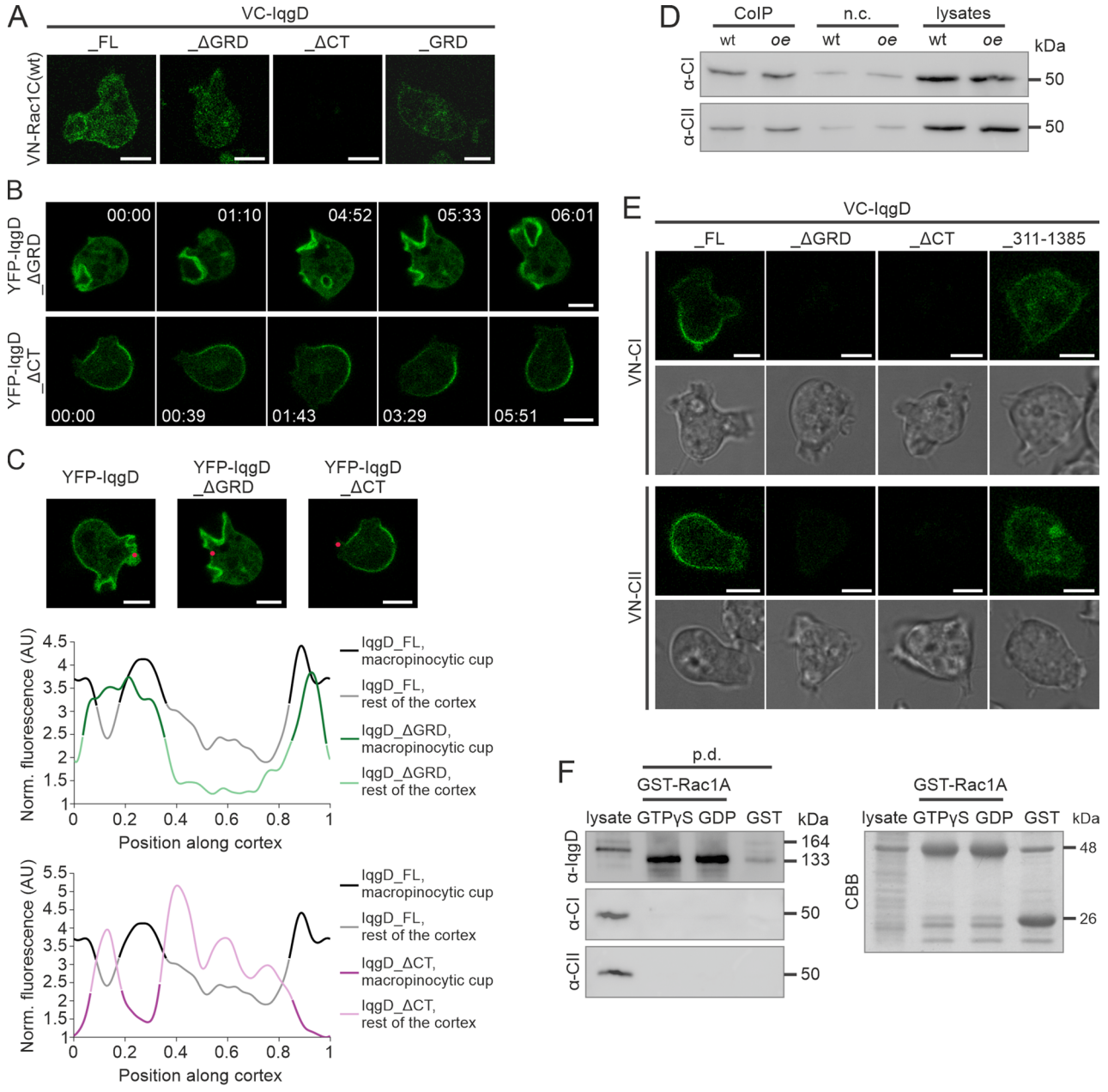


Fig. 6 The GRD and CT domains of IqgD are required for binding to Rac1 and cortexillin. **A** Images of vegetative *iqgD*$^{L1-}$ cells expressing VN-Rac1C(wt) with VC-IqgD_FL (full-length), VC-IqgD_ΔGRD, VC-IqgD_ΔCT, or VC-IqgD_GRD. **B** Image sequences of vegetative *iqgD*$^{L1-}$ cells expressing YFP-IqgD_ΔGRD (*upper panel*) and YFP-IqgD_ΔCT (*lower panel*). **C** Fluorescence intensity profiles along the cortex of cells expressing YFP-tagged full-length IqgD and truncated variants lacking the GRD or CT domain. For easier comparison, cells with similar morphology were used: frame 05:51 from Fig. 2B for IqgD_FL, frame 05:33 from the upper panel of Fig. 6B for IqgD_ΔGRD, and frame 00:00 from the lower panel of Fig. 6B for IqgD_ΔCT (*upper panel*). Red dots indicate starting points from which signal intensities were measured in a clockwise direction. Profiles from cells expressing YFP-IqgD_ΔGRD (*upper line plot*) and YFP-IqgD_ΔCT (*lower line plot*) were circularly shifted relative to the profile of YFP-IqgD_FL to align cortical domains, i.e. macropinocytic cups and the rest of the cortex. Fluorescence profiles were interpolated onto a common normalised cortical coordinate. **D** Anti-CI (*upper membrane*) and anti-CII (*lower membrane*) blots of co-immunoprecipitation of cortexillins I and II with IqgD from lysates of wild-type (wt) and IqgD-overexpressing (*oe*) cells (*CoIP*). Co-immunoprecipitation with non-specific IgG was performed as a negative control (*n.c.*). **E** Images of *iqgD*$^{L1-}$ cells co-expressing either VN-CI (*two upper panels*) or VN-CII (*two lower panels*) with VC-IqgD_FL, VC-IqgD_ΔGRD, VC-IqgD_ΔCT, or VC-IqgD_311–1385. **F** Anti-IqgD blot (*upper membrane*) of GST-Rac1A pull-down shows that IqgD_311–1385 bound to both GTPγS- and GDP-loaded Rac1A. However, CI or CII from lysates of *dgap1*$^{-}$*/gapA*$^{-}$ cells did not associate with IqgD_311–1385, as shown by the anti-CI (*middle membrane*) and anti-CII (*lower membrane*) blots (*left*). The CBB-stained PAG of GST proteins used in the pull-down assay is shown (*right*). In (**B**), time is shown in min: sec format. Scale bars: 5 µm. **B** corresponds to Videos 5 and 6

IqgD is required for normal growth on bacterial lawns

Since IqgD is distributed throughout the cortex with strong enrichment in macroendocytic cups, we compared the efficiency of fluid and particle uptake, as well as other actin-driven processes, in wild-type and IqgD-deficient cells. As *iqgD*$^{L1-}$ cells express negligible amounts of IqgD (Fig. S2C), we used them for most experiments. First, we examined the growth of *iqgD*$^{L1-}$ cells in suspension. Although they grew slightly faster than wild-type cells, the difference was not statistically significant (Fig. 7A). Consistent with this, *iqgD*$^{L1-}$ cells did not show increased macropinocytosis efficiency (Fig. 7B), and the size of their macropinosomes was not significantly different from that of wild-type cells (Fig. 7C). Growth in suspension and macropinosome size were compared for three and two *iqgD*$^{L1-}$ clones, respectively, to demonstrate the consistency of the phenotype among independent clones. Next, we analysed the growth of

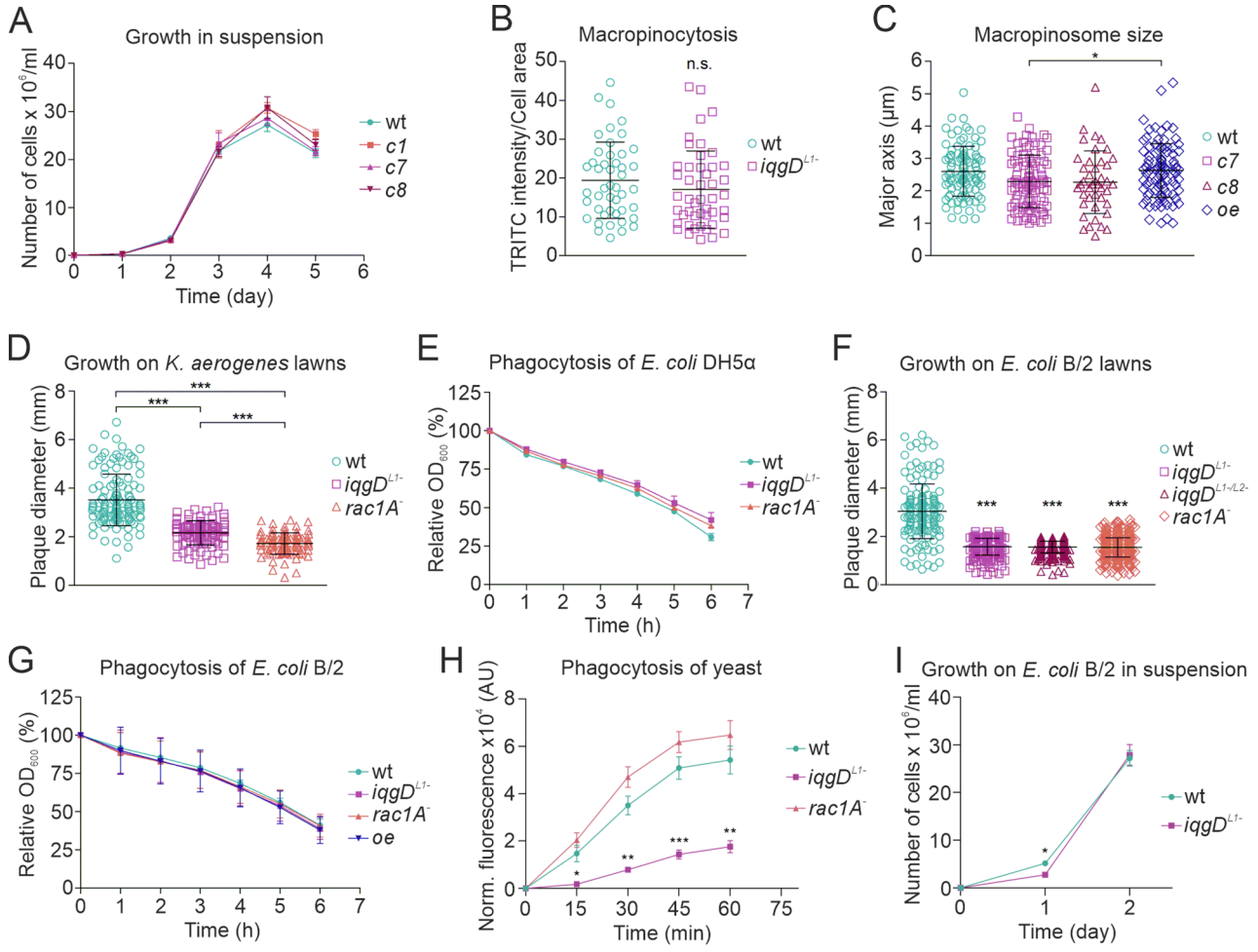


Fig. 7 *IqgD*$^{L1-}$ cells exhibit a severe growth defect on bacterial lawns. **A** *IqgD*$^{L1-}$ cells (clones *c1*, *c7*, and *c8*) grow at a rate similar to wild-type (wt) cells in shaken liquid culture medium ($n \geq 6$, mean ± SEM). **B** There is no statistically significant difference in fluid uptake between wt and *iqgD*$^{L1-}$ cells. Data show the results of one of four experiments in which the ratios of TRITC intensity to cell area were: 19.4 ± 9.9 for wt, $n = 46$; and 17 ± 10 for *iqgD*$^{L1-}$, $n = 47$ (mean ± SD). **C** Macropinosomes of *iqgD*$^{L1-}$ cells (*c7* and *c8*) are slightly smaller than those of wt cells, while cells expressing YFP-IqgD (*oe*) have macropinosomes indistinguishable from wt cells. The length of the macropinosome major axis, determined from at least 3 independent experiments, was: 2.6 ± 0.8 µm for wt, $n = 97$; 2.3 ± 0.8 µm for *iqgD*$^{L1-}$, *c7*, $n = 92$; 2.3 ± 1 µm for *iqgD*$^{L1-}$, *c8*, $n = 42$; and 2.6 ± 0.8 µm for *oe*, $n = 95$ (mean ± SD). **D** *IqgD*$^{L1-}$ and *rac1A*$^-$ cells grow significantly more slowly than wt cells on solid plates with *K. aerogenes* as the food source. The diameters of plaques from 4 independent experiments measured on day 4 were: 3.5 ± 1.1 mm for wt, $n = 123$; 2.2 ± 0.5 mm for *iqgD*$^{L1-}$, $n = 98$; and 1.7 ± 0.4 mm for *rac1A*$^-$, $n = 93$ (mean ± SD). **E** *IqgD*$^{L1-}$ and *rac1A*$^-$ cells show similar efficiency in phagocytosis of *E. coli* DH5α from shaken suspension as wt cells ($n \geq 3$, mean ± SEM). **F** *IqgD*$^{L1-}$, *iqgD*$^{L1-/L2-}$, and *rac1A*$^-$ cells grow significantly more slowly than wt cells on solid plates with *E. coli* B/2 as the food source. The diameters of plaques from 4 independent experiments measured on day 5 were: 3 ± 1.1 mm for wt, $n = 154$; 1.6 ± 0.4 mm for *iqgD*$^{L1-}$, $n = 231$; 1.6 ± 0.2 mm for *iqgD*$^{L1-/L2-}$, $n = 356$; and 1.5 ± 0.4 mm for *rac1A*$^-$, $n = 438$ (mean ± SD). **G** *IqgD*$^{L1-}$, *rac1A*$^-$, and *oe* cells show similar efficiency in phagocytosis of *E. coli* strain B/2 from shaken suspension as wt cells ($n \geq 5$, mean ± SEM). **H** *IqgD*$^{L1-}$ cells show markedly reduced uptake of yeast particles compared to wt and *rac1A*$^-$ cells ($n = 6$, mean ± SEM). **I** *IqgD*$^{L1-}$ cells grow at a rate similar to wt cells in suspension with bacteria as the food source ($n = 3$, mean ± SEM). Statistical analyses were performed using: two-way RM ANOVA with Bonferroni post-tests in (**A**), (**E**), (**G**), (**H**), and (**I**); Mann-Whitney test in (**B**); Kruskal-Wallis test followed by Dunn's multiple comparison test for pairwise comparisons in (**C**), (**D**), and (**F**). The significance level was set at 5% for all analyses. n.s. – not significant, * $P < 0.05$, ** $P < 0.01$, *** $P < 0.001$

iqgD^{L1-} cells on a lawn of *K. aerogenes* and found that they formed markedly smaller plaques than wild-type cells (Fig. 7D). Assuming that IqgD functions as a Rac1 effector, we compared the growth of *iqgD*$^{L1-}$ and *rac1A*$^{-}$ cells. We used *rac1A*$^{-}$ cells because Rac1A is the most highly expressed Rac1 isoform in vegetative AX2 cells [54, 55]. The *rac1A*$^{-}$ cells were generated by homologous recombination, and successful inactivation of the *rac1A* gene was confirmed by PCR and Southern blot (Fig. S6). As expected, *rac1A*$^{-}$ cells grew significantly more slowly than both wild-type and *iqgD*$^{L1-}$ cells on bacterial lawns (Fig. 7D). Because slow growth on bacterial lawns is most likely caused by inefficient phagocytosis of bacteria, we examined the uptake of *E. coli* strain DH5α in suspension. Unexpectedly, however, neither *iqgD*$^{L1-}$ nor *rac1A*$^{-}$ cells showed reduced uptake of bacteria (Fig. 7E). To exclude potential effects arising from the use of different bacterial species for growth on bacterial lawns and phagocytosis in suspension, we repeated both assays with *E. coli* strain B/2, which is considered suitable for phagocytosis under both conditions. Again, we observed significantly reduced growth rates for *iqgD*$^{L1-}$ and *rac1A*$^{-}$ cells compared to wild-type cells on bacterial lawns (Fig. 7F), whereas *iqgD*$^{L1-}$, *rac1A*$^{-}$, IqgD-overexpressing, and wild-type cells all showed similar phagocytosis efficiency in suspension (Fig. 7G). We also included *iqgD*$^{L1-/L2-}$ double knockout cells and found no difference in plaque size between *iqgD*$^{L1-}$ and *iqgD*$^{L1-/L2-}$ cells (Fig. 7F). Interestingly, phagocytosis of yeast particles from suspension was markedly diminished in *iqgD*$^{L1-}$ cells, whereas *rac1A*$^{-}$ cells phagocytosed yeasts with efficiency comparable to wild-type cells (Fig. 7H). To test whether the poor growth of *iqgD*$^{L1-}$ cells on bacterial lawns reflects a defect in bacterial processing after uptake, we measured growth in *E. coli* B/2 suspension. Although mutant cells reached a slightly lower density than wild-type cells after one day of growth, by the second day, mutant and wild-type cultures reached comparable cell densities (Fig. 7I). We conclude that, despite a transient delay during the initial phase of growth, *iqgD*$^{L1-}$ cells do not show a sustained defect in growth on bacteria in suspension. This suggests that the impaired growth on bacterial lawns may reflect a defect specific to the growth conditions within the bacterial lawn on agar.

IqgD is required for phagocytosis of surface-attached particles

As *iqgD*$^{L1-}$ cells showed no cytokinesis defect when grown on Petri dishes, we examined cell motility and adhesion to identify other possible reasons for their poor growth on bacterial lawns. Randomly moving vegetative *iqgD*$^{L1-}$ cells displayed only a slightly increased speed and unchanged directional persistence compared to wild-type cells (Fig. 8A and Video 7). However, their adhesion to the substrate was significantly reduced compared to wild-type cells (Fig. 8B). *Rac1A*$^{-}$ cells exhibited an even more pronounced defect in cell-substrate adhesion. Using total internal reflection fluorescence (TIRF) microscopy, we then investigated whether IqgD localises to adhesion foci, but instead found it to be evenly distributed throughout the ventral cortex (Video 8). Impaired adhesion during growth on bacterial lawns could affect cytokinesis, phagocytosis, or motility, even if these processes appear unaffected under other conditions. Therefore, we harvested cells from the vegetative zone of the spreading plaque, fixed them, and stained them with DAPI. Most wild-type and *iqgD*$^{L1-}$ cells were mononucleated, with a very small proportion of binucleated cells that did not differ statistically between the cell lines (wt 2.3%, $n = 174$; *iqgD*$^{L1-}$ 0.65%, $n = 154$). However, the measured cell area of *iqgD*$^{L1-}$ cells was significantly smaller than that of wild-type cells (Fig. 8C). Based on these results, we hypothesised that *iqgD*$^{L1-}$ cells have a specific defect in phagocytosis of bacteria attached to the agar surface, possibly involving a mechanism similar to that used by macrophages to detach and internalise surface-bound particles [46]. Macrophages form an F-actin-rich circular adhesive structure, termed the phagocytic adhesion ring (PAR), around the particle at the cell-substrate interface, which provides the force for its detachment from the surface. To investigate whether a similar structure exists in *Dictyostelium*, we plated wild-type cells expressing an F-actin probe on a glass surface covered with silicone grease droplets. Interestingly, F-actin encircled the droplets underneath the cell in a manner similar to PARs in macrophages (Fig. 8D and Video 9). We then found that IqgD and active Rac1 also localise to this structure (Fig. 8D, and Videos 10 and 11). However, active Rac1 consistently formed discrete, narrow rings around droplets, whereas F-actin displayed more heterogeneous localisation patterns, ranging from discrete rings to broader, more dispersed signals around droplets that decreased radially from the droplet. IqgD exhibited a localisation pattern similar to F-actin. Notably, both IqgD_ΔGRD and IqgD_ΔCT were able to localise to these ventral rings, although localisation of IqgD lacking the CT was observed only very rarely and generally with a significantly lower signal (Fig. 8D).

To investigate the relevance of IqgD in the phagocytosis of surface-bound particles, we adapted a recently described protocol developed for macrophages [46]. Wild-type, *iqgD*$^{L1-}$, and IqgD-overexpressing cells were plated on a poly-L-lysine-coated glass surface to which 1 µm fluorescent beads had been immobilised. After 30 min, the cells were fixed and the number of ingested particles was determined using confocal microscopy. Notably, *iqgD*$^{L1-}$ cells phagocytosed significantly fewer particles than wild-type cells (Fig. 8E), strongly

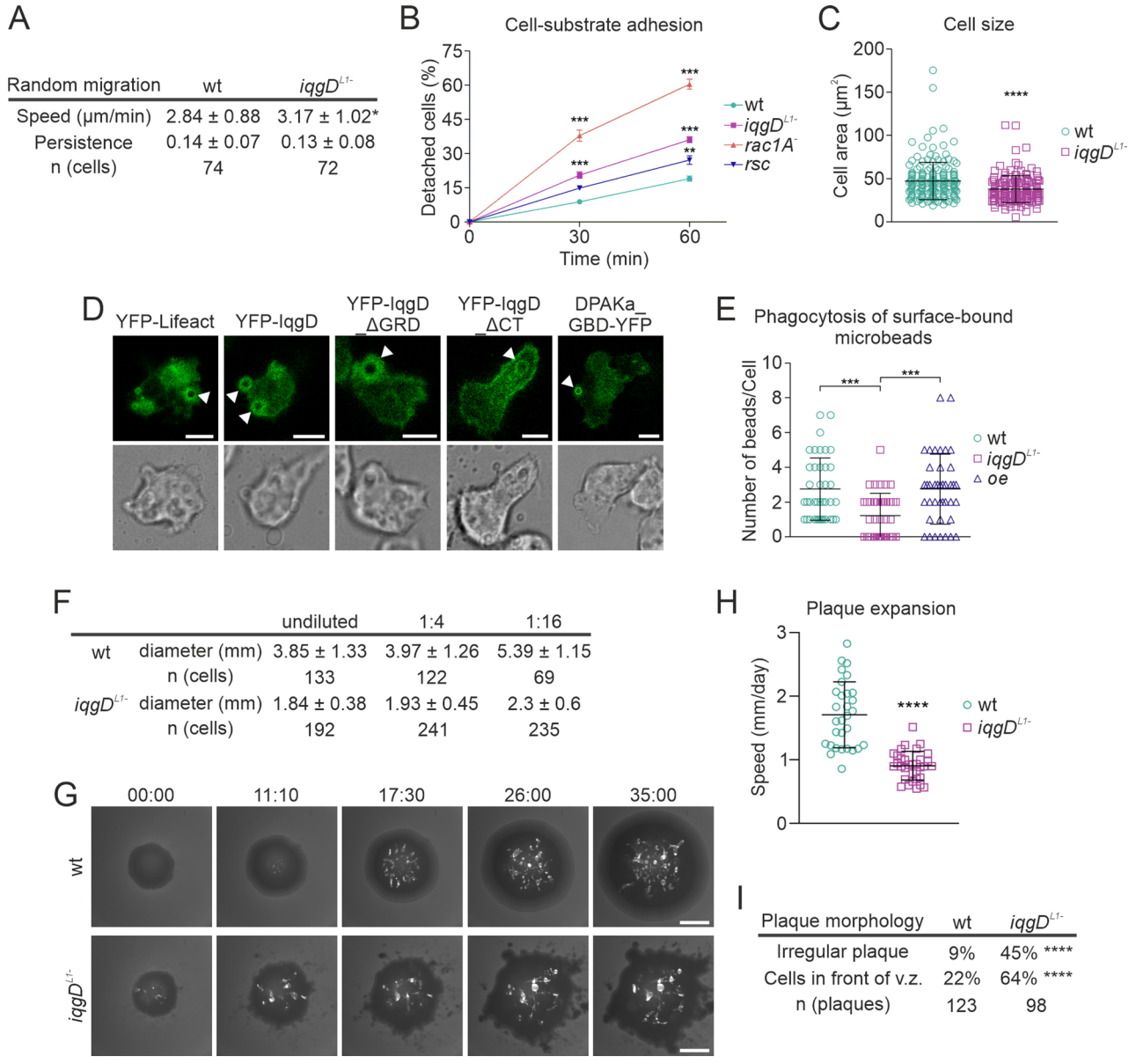


Fig. 8 *lqgD*$^{L1-}$ cells display impaired phagocytosis of surface-bound particles and irregular plaque expansion on *K. aerogenes* lawns. **A** The speed of randomly moving *iqgD*$^{L1-}$ cells is slightly increased compared to wild-type (wt) cells, while persistence is not altered. Data are from 4 independent experiments (mean ± SD). **B** *lqgD*$^{L1-}$ and *rac1A*$^{-}$ cells are less strongly attached to the substrate than wt cells in a detachment assay ($n \geq 4$, mean ± SEM). Expression of exogenous YFP-lqgD in *iqgD*$^{L1-}$ cells (*rsc*) partially rescues their adhesion defect. **C** *lqgD*$^{L1-}$ cells harvested from the vegetative zone of the plaque on a *K. aerogenes* lawn are significantly smaller than their wild-type counterparts. The cell areas from 3 independent experiments were: 47.2 ± 21.4 μm^2 for wt, $n = 174$; and 37.8 ± 15.5 μm^2 for *iqgD*$^{L1-}$, $n = 154$ (mean ± SD). **D** Confocal images of the ventral surface of wild-type cells expressing YFP-Lifeact, YFP-lqgD, YFP-lqgD_ΔGRD, YFP-lqgD_ΔCT, and DPAKa_GBD-YFP. The cells were attached to the glass surface covered with silicone grease droplets of various sizes in the micrometre range. **E** *lqgD*$^{L1-}$ cells are less efficient than wild-type cells in phagocytosis of surface-bound 1 μm beads. The numbers of ingested beads in 30 min were: 2.8 ± 1.8 for wt, $n = 40$; 1.2 ± 1.3 for *iqgD*$^{L1-}$, $n = 40$; and 2.8 ± 2 for *oe* cells, $n = 40$ (mean ± SD). **F** Diameters of both wt and *iqgD*$^{L1-}$ plaques increase as *K. aerogenes* density decreases within a lawn ($n \geq 4$, mean ± SD). **G** Time-lapse image sequences show typical wt and *iqgD*$^{L1-}$ plaque spreading on *K. aerogenes* lawns. **H***lqgD*$^{L1-}$ plaques expanded at nearly half the rate of wild-type plaques. Plaque expansion rates were determined by measuring plaque diameters on consecutive days starting from day 3. The expansion rate was 1.71 ± 0.52 mm/day for wild-type plaques and 0.91 ± 0.23 mm/day for *iqgD*$^{L1-}$ plaques ($n = 6$; mean ± SD). **I** *lqgD*$^{L1-}$ cells more frequently form plaques with an irregular front and escape ahead of the vegetative zone forming satellite plaques (*Cells in front of v.z.*). Plaque morphology was compared between wt and *iqgD*$^{L1-}$ cells in 4 independent experiments. In (**G**) time is shown in hours: min format. Scale bars: (**D**) 5 μm; (**G**) 1 mm. Statistical analyses were performed using: Mann-Whitney test in (**A**), (**C**), and (**H**); two-way RM ANOVA with Bonferroni post-tests in (**B**); Kruskal-Wallis test followed by Dunn's multiple comparison test for pairwise comparisons in (**E**); unpaired t-test with Welch's correction in (**H**). The significance level was set at 5% for all analyses. * $P < 0.05$, ** $P < 0.01$, *** $P < 0.001$, **** $P < 0.0001$. Images of cells expressing YFP-Lifeact, YFP-lqgD and DPAKa_GBD-YFP in (D) correspond to Videos 9–11. Sequences in (**G**) correspond to Videos 12 and 13

suggesting that their reduced growth on bacterial lawns could be, at least partly, due to inefficient phagocytosis of bacteria attached to the surface. As bacterial lawns consist of multiple layers of bacteria, it is unlikely that a defect in phagocytosis of surface-attached bacteria alone can fully account for the overall reduced growth on bacterial lawns. Therefore, we investigated whether thinning the bacterial multilayer affects plaque size. We plated wild-type and *iqgD*$^{L1-}$ cells on SM agar containing decreasing initial densities of *K. aerogenes*. Both cell lines formed larger plaques on less dense bacterial lawns, although the increase in plaque diameter between undiluted and 16-fold diluted bacteria was somewhat greater for wild-type than for *iqgD*$^{L1-}$ cells (40% vs. 25%, Fig. 8F). Next, we monitored the expansion of individual plaques by microscopy. This initial analysis suggested that, once visible, *iqgD*$^{L1-}$ plaques expanded at a rate fairly comparable to wild-type plaques (Fig. 8G). To quantify plaque expansion more precisely, we plated wild-type and *iqgD*$^{L1-}$ cells on *K. aerogenes* lawns and measured plaque diameters daily for four days from day 3. By comparing the slopes of growth curves for individual plaques, we found that *iqgD*$^{L1-}$ plaques expanded at a substantially lower rate than wild-type plaques (Fig. 8H). In addition, *iqgD*$^{L1-}$ plaques often exhibited a highly irregular vegetative zone, with many cells escaping ahead of the plaque front (Fig. 8G and I, Videos 12 and 13). Interestingly, this effect was observed on *K. aerogenes* lawns, but not on *E. coli* B/2. Together, these results indicate that IqgD is required for normal growth on bacterial lawns and for normal organisation of the vegetative front on *K. aerogenes* lawns.

Cortexillins functionally cooperate with IqgD during growth on bacterial lawns

We have shown that IqgD interacts directly with active Rac1, F-actin, and cortexillin I and II. However, IqgD is not essential for their overall subcellular localisation, as active Rac1 (Fig. 9A) and F-actin (Fig. S3C and Fig. 9B) display the same distribution in both wild-type and *iqgD*$^{L1-}$ cells. The cortical localisation of CI and CII is also unaffected in *iqgD*$^{L1-}$ cells (Fig. 9C). To functionally connect IqgD and cortexillins, we examined the growth of CI-deficient (*ctxA*$^{-}$), CII-deficient (*ctxB*$^{-}$), and CI/CII-deficient (*ctxA*$^{-}$/*ctxB*$^{-}$) cells on bacterial lawns. Similar to *rac1A*$^{-}$ cells (Fig. 7D and F), *ctxA*$^{-}$ and *ctxA*$^{-}$/*ctxB*$^{-}$ cells also exhibit markedly reduced growth on bacterial lawns, as do *iqgD*$^{L1-}$ cells, whereas *ctxB*$^{-}$ cells do not show any defect on bacterial lawns (Fig. 9D). However, both single *ctxA*$^{-}$ and *ctxB*$^{-}$ mutants show significantly decreased phagocytosis of surface-attached microbeads, while the *ctxA*$^{-}$/*ctxB*$^{-}$ double mutant displays an even more pronounced defect (Fig. 9E). The similar phenotypes of *rac1A*$^{-}$, *iqgD*$^{L1-}$, and cortexillin mutant cells, together with the physical interactions between IqgD and Rac1 and between IqgD and cortexillins, support a model in which Rac1, IqgD, and cortexillins act together to facilitate the uptake of bacteria attached to the surface of the agar plate and to ensure overall efficient growth of *D. discoideum* cells on bacterial lawns.

Discussion

In this study, we set out to define the cellular role of the IQGAP-related protein IqgD from *D. discoideum*. Given that IqgD contains CHD, GRD, RGCT, and CT domains that, in human IQGAP1, mediate interactions with F-actin and the Rho GTPases Cdc42 and Rac1, we investigated whether IqgD similarly interacts with F-actin and Rho family GTPases in *D. discoideum*. We show that IqgD localises to F-actin-rich structures such as the cell cortex and macroendocytic cups, and that its cortical localisation depends on an intact actin cortex and the presence of the CHD. Consistent with this localisation, we found that IqgD binds directly to F-actin, although this interaction appears to be of relatively low affinity, at least when using rabbit skeletal muscle actin, as assessed by co-sedimentation assays using an N-terminal fragment containing the CHD. In contrast, Hoeprich et al. reported that a monomeric N-terminal fragment of human IQGAP1 containing the CHD is sufficient for stable binding along filament sides [27]. Its dwell time appears comparable to that of the dimeric full-length protein, and both full-length human IQGAP1 and the N-terminal fragment bind to filament sides with high affinity. By contrast, the relatively low binding affinity of IqgD may be explained by the presence of a different type of CHD compared with that in IQGAP1. Mammalian IQGAPs contain a single type 3 CHD, whereas IqgD harbours two fimbrin-type CHDs, CHf1 and CHf2 [56, 57]. Fimbrins are potent actin-bundling proteins that contain two CHD duplexes, which together constitute two actin-binding domains (ABDs) [56]. In general, both fimbrins and IQGAPs exhibit moderate to high binding affinity for F-actin sides [27, 58–62]. However, in contrast to canonical fimbrins, IqgD harbours only one duplex and was therefore originally referred to as a fimbrin-related RasGAP [57]. Notably, it is well established that the ABDs of fimbrin differ in their binding affinities for F-actin, with the isolated ABD2 binding substantially more strongly than ABD1 [62–64]. Accordingly, the presence of only the first two CHDs of fimbrin, corresponding to ABD1, in IqgD may account for its relatively low affinity for F-actin. Unfortunately, the low yield of IqgD_1-592 from insect cells precluded assessment of its bundling activity in a low-speed actin spin-down assay.

We further show that IqgD interacts with the *D. discoideum* orthologues of human Rac1, namely the GTPases Rac1A, Rac1B, and Rac1C [65]. Although IqgD binds

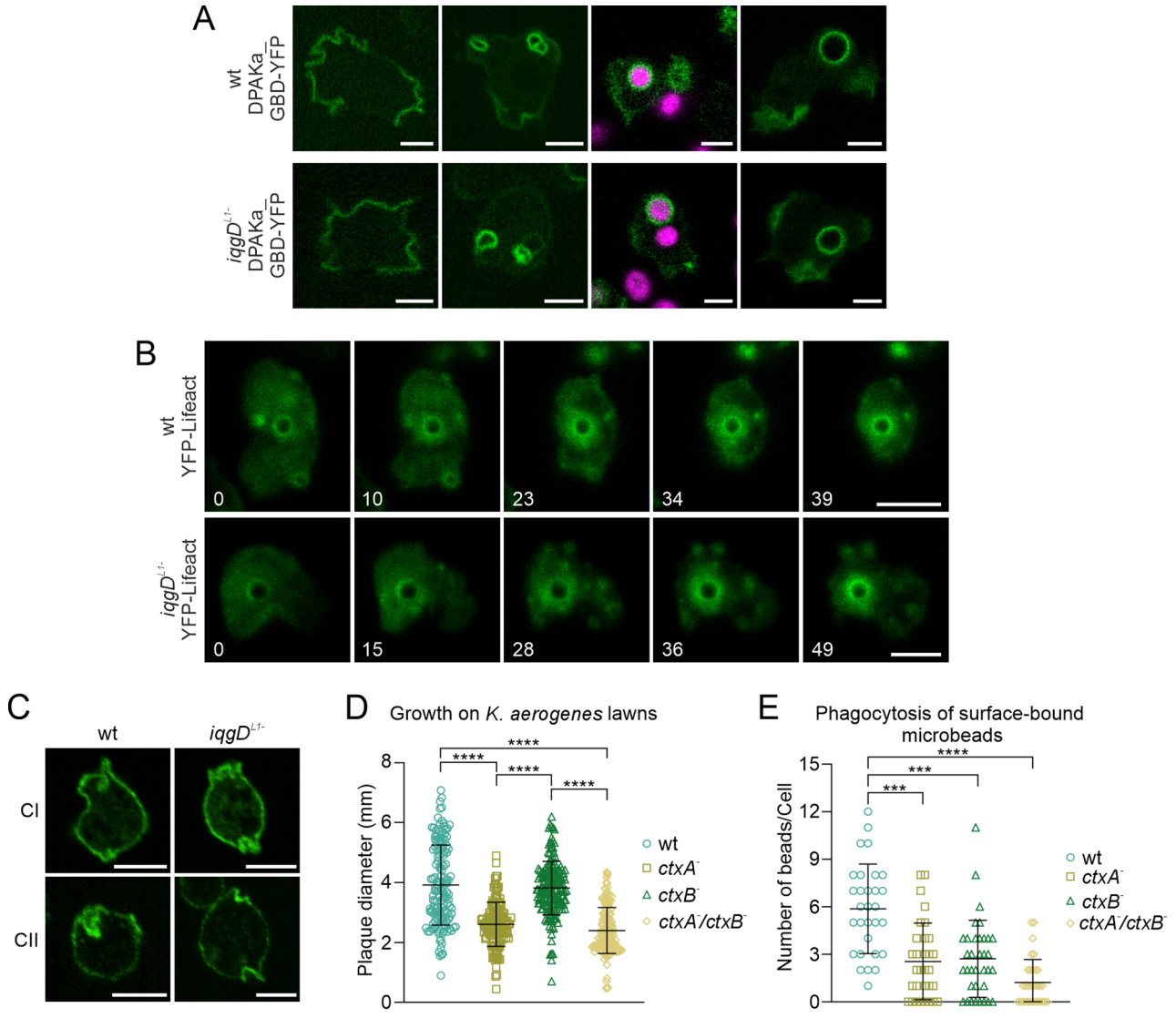


Fig. 9 Cells deficient in cortexillins display phenotypes similar to *iqgD*$^{L1-}$ cells. **A** Localisation of the probe for active Rac1 GTPases, DPAKa_GBD-YFP, in wild-type (wt, *upper panel*) and *iqgD*$^{L1-}$ (*lower panel*) cells in the cell cortex, on macropinosomes, on the phagosome, and around surface-attached silicone grease droplets. **B** Image sequence of wt (*upper panel*) and *iqgD*$^{L1-}$ (*lower panel*) cells expressing the probe for F-actin, YFP-Lifeact, which localises around surface-attached silicone grease droplets. **C** Representative images of wt and *iqgD*$^{L1-}$ cells immunostained with anti-CI (*upper panel*) and anti-CII (*lower panel*) antibodies. **D***CtxA*$^-$*and ctxA*$^-$*/ctxB*$^-$ cells grow significantly more slowly than wt cells on solid plates with *K. aerogenes* as the food source. The diameters of plaques from at least 4 independent experiments measured on day 4 were: 3.9 ± 1.3 mm for wt, $n = 150$; 2.6 ± 0.7 mm for *ctxA*$^-$, $n = 134$; 3.8 ± 0.9 mm for *ctxB*$^-$, $n = 174$; and 2.4 ± 0.8 mm for *ctxA*$^-$*/ctxB*$^-$ cells, $n = 177$ (mean ± SD). **E** Single *ctxA*$^-$, single *ctxB*$^-$, and double *ctxA*$^-$*/ctxB*$^-$ mutant cells are less efficient than wt cells in phagocytosis of surface-bound 1 µm beads. The numbers of ingested beads in 30 min were: 5.9 ± 2.8 for wt, $n = 30$; 2.5 ± 2.4 for *ctxA*$^-$, $n = 31$; 2.7 ± 2.4 for *ctxB*$^-$, $n = 35$; and 1.2 ± 1.5 for *ctxA*$^-$*/ctxB*$^-$ cells, $n = 32$ (mean ± SD). In (**B**), time is shown in seconds. Scale bars: 5 µm. Statistical analyses were performed using the Kruskal-Wallis test followed by Dunn's multiple comparison test for pairwise comparisons in (**D**) and (**E**). The significance level was set at 5% for all analyses. *** $P < 0.001$, **** $P < 0.0001$

more strongly to inactive Rac1A in GST-Rac1A pull-down assays, BiFC analysis shows that it interacts exclusively with active Rac1 GTPases in living cells. This, together with the finding that IqgD does not function as a GAP for Rac1 GTPases, suggests that it acts as a Rac1 effector. Consistent with this, the phenotype of *iqgD*$^{L1-}$ cells overlaps with that of *rac1A*$^-$ cells. However, cell adhesion and growth on *K. aerogenes* lawns are more severely impaired in the absence of Rac1A than in the absence of IqgD, probably because Rac1A functions as an upstream regulator that signals through multiple downstream effectors in distinct pathways.

IqgD is present in various F-actin-based structures, including protrusive structures such as macropinocytic and phagocytic cups, where it is highly enriched, as well as in retractive cortical structures. Notably, IqgD does not localise to the polar protrusions of separating daughter cells during cytokinesis or to the pseudopods

of migrating cells, where strong F-actin polymerisation occurs [66, 67]. The CHD is essential for overall cortical localisation through its ability to bind F-actin, as an IqgD variant lacking the CHD is largely cytosolic. However, truncated IqgD variants that retain the CHD but lack either the GRD or the CT domain display distinct cortical distributions: IqgD_ΔGRD is restricted to macropinocytic cups, whereas IqgD_ΔCT is found in the remaining, non-cup cortical regions. Thus, while the CHD mediates general cortical attachment, the GRD and CT domains further specify distinct cortical localisations. The RGCT domains of human IQGAP1 and IQGAP2 exhibit approximately 100-fold higher affinity for active than for inactive Cdc42 in vitro, whereas their GRDs bind Cdc42 with low affinity independent of the nucleotide state [2]. Based on these findings, the RGCT domain has been proposed to function as the actual effector domain or GTPase-binding domain (GBD) of IQGAP, with the GRD serving mainly as a scaffold for the GTPase [2, 22]. We show that the GRD and CT domains of IqgD contribute to Rac1 binding, with the CT domain playing a critical role, as IqgD lacking the CT fails to interact with Rac1C in a BiFC assay. This result can be explained by recent interaction studies using purified GTPases and fragments of mammalian IQGAPs [22, 68]. It was shown that a construct lacking the CT domain (GRD-RGCT) had a 4–6-fold faster k_{off} compared to GRD-RGCT-CT when interacting with Rac1, suggesting that the CT stabilises the overall interaction [22]. Similarly, a decisive role of the CT domain in stabilising the interaction between IqgD and Rac1 in living cells is implied by our BiFC experiments. Additionally, we show that IqgD interacts with the actin-bundling proteins cortexillin I and II, but not simultaneously with Rac1. This mutually exclusive binding is consistent with the finding that cortexillins bind to IqgD through the same GRD and CT domains. However, further experiments are required to explain the distinct localisation patterns of IqgD_ΔGRD and IqgD_ΔCT. It would also be valuable to test the contribution of the recently redefined RGCT domain of IqgD to these interactions in future [35].

Despite its striking localisation at macropinocytic and phagocytic cups, IqgD does not appear to be required for macropinocytosis or for phagocytosis of bacteria from suspension. In contrast, it is critical for efficient phagocytosis of yeast particles from suspension and for phagocytosis of surface-bound 1 µm beads. Recent work has revealed the mechanism by which macrophages internalise surface-bound particles [46]. When a macrophage encounters a particle beneath its cell body, it forms an F-actin-rich circular structure around the particle at the cell-substrate interface. This structure is both adhesive and phagocytic, as it contains integrin β_2, talin, vinculin, F-actin, Arp3, pFAK (phosphorylated focal adhesion kinase), and Rab5a [69, 70], and has therefore been termed the phagocytic adhesion ring (PAR) [46]. The authors proposed a model for PAR-mediated phagocytosis in which macrophages sense a surface-attached particle through disruption of continuous waves of actin polymerisation at the basal cell surface. This interference triggers PAR formation, and integrins within the PAR support inward Arp2/3-mediated actin polymerisation towards the particle-substrate interface, generating the force required for particle detachment from the substrate and subsequent phagocytosis [46]. Because phagocytosis is an evolutionarily conserved process, with *D. discoideum* serving as a well-established macrophage-like model [71], we hypothesise that *D. discoideum* may form a PAR-like structure during uptake of surface-bound particles. Using silicone grease droplets to mimic surface-bound particles, we show that *D. discoideum* cells also assemble a circular F-actin-containing structure around particles at the basal cell surface. We further demonstrate that IqgD and Rac1A are components of this structure. Finally, we show that *iqgD*$^{L1-}$ cells phagocytose significantly fewer surface-bound beads compared to wild-type cells. These findings support the idea that IqgD is required for efficient phagocytosis of surface-attached bacteria on bacterial lawns. Nevertheless, in a fully grown multilayered lawn, bacteria directly attached to the agar surface make up only a small fraction of the total bacterial biomass. Therefore, inefficient phagocytosis of agar-attached bacteria is unlikely, by itself, to account for the overall reduced growth of *iqgD*$^{L1-}$ cells on bacterial lawns. We propose that the defect in phagocytosis of surface-attached bacteria may contribute to the initial delay in plaque formation, during the first hours after plating, when the bacterial layer is still thin and a larger fraction of bacteria is presumably attached to the agar surface. However, cells from the vegetative zone of expanding *iqgD*$^{L1-}$ plaques are moderately smaller than wild-type cells, indicating a sustained defect in feeding. Consistent with this phenotype, *iqgD*$^{L1-}$ plaques expand at approximately half the rate of wild-type plaques. Although little is known about bacterial lawns, they may behave similarly to biofilms. It is known that *K. aerogenes* can adhere to the surface and form biofilms, and that bacterial extracellular polymeric substances promote attachment and mechanical stability of the biofilm community [72]. In addition, *D. discoideum* has been shown to feed on biofilms formed by *E. coli* and *Klebsiella oxytoca* [73]. It is possible that bacteria in a lawn also produce an extracellular matrix in which bacteria may be partially immobilised or form cohesive microclusters. Material integrity of the *K. aerogenes* lawn was also recently suggested in a study exploring the interaction of the advancing vegetative zone and bacterial population [74]. Feeding on such densely packed bacteria could impose greater mechanical

demands on the phagocytic cup than uptake of bacteria suspended in solution. This interpretation is consistent with the strongly reduced uptake of large particles by *iqgD*$^{L1-}$ cells. Therefore, we propose that IqgD plays a crucial role when engulfment requires a more extensive phagocytic cup, as during phagocytosis of yeast particles, or force generation, as during phagocytosis of surface-attached particles and, presumably, strongly interconnected bacteria within a lawn.

In addition, plaques formed by *iqgD*$^{L1-}$ cells on *K. aerogenes* lawns were frequently highly irregular, with many satellite plaques forming outside the original plaque. A similar phenotype was reported for *cadA*$^{-}$ cells grown on *K. pneumoniae* lawns [75]. CadA is a cell adhesion protein that functions during development, but it is also a bacterial agglutinin essential for proper organisation of the vegetative zone and for establishing a protective interface between amoebae and bacteria [76, 77]. However, unlike *cadA*$^{-}$ cells, which exhibited poor viability during the initial stages of plaque formation when plated with a dense bacterial population, *iqgD*$^{L1-}$ cells did not show a viability defect. These data suggest that IqgD contributes to maintaining an organised feeding front on *K. aerogenes* lawns. This phenotype may reflect reduced adhesion of *iqgD*$^{L1-}$ cells, allowing some cells to penetrate areas of the lawn where local bacterial density or mechanical resistance is lower. Interestingly, this effect was not observed on *E. coli* lawns or with *rac1A*$^{-}$ or *ctxA*$^{-}$ cells, suggesting an *iqgD*$^{L1-}$-specific phenomenon that depends on the physical or chemical properties of the bacterial lawn. Similarly, the viability defect of *cadA*$^{-}$ cells was observed on *K. pneumoniae* lawns, but not when cells were plated with *Micrococcus luteus*, *Bacillus subtilis*, or *Staphylococcus aureus* [75].

IqgD and its direct binding partners, active Rac1 and F-actin, are enriched at macroendocytic cups compared with the rest of the cortex. Immunofluorescence imaging suggests that CII is also enriched at macroendocytic cups, whereas CI appears uniformly distributed across the entire cortex. This is consistent with a previous study describing the localisation of cortexillins in vegetative cells [53]. Of note, CI and CII localise to the posterior cortex of polarised cells [78]. However, despite the enrichment of IqgD and its binding partners at cup regions, BiFC experiments suggest that IqgD is more engaged in interactions with both Rac1 and cortexillins in the retractive, non-cup cortical regions. Weaker BiFC signals from the interaction between IqgD and Rac1A/Rac1B in the cup region than in the rest of the cortex suggest that IqgD and Rac1 are less engaged with each other and more with other binding partners in macroendocytic cups. This further implies that, in the cups, IqgD preferentially associates with F-actin and/or cortexillins. Based on the biochemical and interaction data, we propose that IqgD affects F-actin through at least two mechanisms: directly by binding filament sides via the CHD, and indirectly through its interaction with cortexillins. Consistent with this hypothesis, we find that IqgD does not alter the overall cellular F-actin content, suggesting that, unlike human IQGAP1, IqgD is unlikely to regulate actin polymerisation at the filament barbed end [27, 28]. This aligns with the proposed function of IqgD in mechanically demanding forms of phagocytosis, where IqgD, either directly or through cortexillins, may organise filaments into linear bundles or dense meshwork, thus supporting the expansion of larger cups or the generation of greater forces required for phagocytosis of mechanically constrained particles. At the same time, Rac1 interacts with canonical effectors such as Scar/WAVE to promote Arp2/3-dependent dendritic actin polymerisation, which drives membrane protrusion during phagocytic cup formation. In this scenario, IqgD appears to be more strongly engaged with Rac1 GTPases in the remaining cortex, which precludes its interaction with cortexillins. Under these conditions, cortexillins remain available for interaction with DGAP1 and GAPA, which reside exclusively in the retractive cortex of vegetative cells [39, 79]. The proposed model appears inconsistent with BiFC results showing interaction between IqgD and cortexillins predominantly in the non-cup cortical regions. However, BiFC preferentially reports stable and geometrically favourable interactions, whereas interactions in rapidly remodelling macropinocytic cups may be more transient, with a lifetime insufficient for Venus reconstitution [80, 81]. Therefore, the intensity of the BiFC signal should not be interpreted as a direct measure of the strength of native interactions [82]. We conclude that IqgD appears in at least two cortical complexes, with either Rac1 or cortexillin, and its presence in one of them probably depends on the local concentration and/or availability of binding partners. Additionally, similar to mammalian IQGAPs, we also show that IqgD diminishes the GTPase activity of Rac1 in vitro. Therefore, the interaction of IqgD with Rac1 preserves the active conformation of the GTPase, which may be particularly important in the retractive, non-cup cortical regions, where Rac1 activation may be lower than at macroendocytic cups.

Depletion of IqgD, Rac1A, and CI results in a similar phenotype of markedly reduced plaque formation on bacterial lawns. However, because IqgD does not simultaneously bind Rac1 and CI, a simple linear Rac1A-IqgD-CI signalling pathway is unlikely. Rac1A may contribute to growth on bacterial lawns through a parallel pathway. Furthermore, phagocytosis of large particles is greatly diminished in *iqgD*$^{L1-}$ cells, whereas *rac1A*$^{-}$ cells phagocytose yeast particles with efficiency comparable to wild-type cells. Thus, it is likely that IqgD primarily associates with cortexillins, as supported by

co-immunoprecipitation experiments. Rac1 may shift IqgD away from the cortexillin-containing complex in cortical regions where it is not engaged by other effectors. We therefore propose that IqgD acts as a spatially regulated cortical scaffold, rather than as a simple Rac1 effector like DGAP1.

Conclusions

In this study, we identify IqgD as a key player in mechanically demanding forms of phagocytosis, such as the uptake of large particles, surface-bound particles, and potentially bacteria within dense lawns. This makes IqgD particularly important for amoebal feeding in their natural environment, where vegetative cells frequently encounter surface-associated and aggregated bacteria. Similarly, IqgD is required for efficient growth of *Dictyostelium* cells on bacterial lawns. We identify Rac1 GTPases, F-actin, and the actin-binding proteins cortexillin I and cortexillin II as IqgD interactors, providing mechanistic insight into the function of IqgD. Our data suggest that IqgD acts as a spatially regulated scaffold that exists in at least two mutually exclusive cortical complexes, associated either with Rac1 or with cortexillins. Phagocytosis of surface-attached particles has recently been described in mammalian macrophages as a specialised process essential for innate immunity. In both *Dictyostelium* and macrophages, this process involves the formation of an F-actin-rich ring around the substrate-attached particle at the ventral cell surface. Our findings support an important role for IqgD in this process and suggest that force-generating uptake of surface-attached particles is evolutionarily conserved from protozoa to mammals.

Materials and methods

Plasmid vectors

The coding DNA sequence (CDS) of IqgD was amplified by PCR from cDNA prepared from vegetative cells of the *Dictyostelium discoideum* laboratory strain AX2 and cloned into the pUC18 cloning vector. For expression of IqgD in *D. discoideum* cells, either unlabelled or N- and C-terminally labelled with YFP, the CDS of IqgD was amplified by PCR from pUC18_IqgD and inserted into the pDM304 [83], pDM304_N-YFP [84] or pDM304_C-YFP (this work) vectors by ligation-independent cloning (In-Fusion HD Cloning Kit, Takara Bio). For expression of YFP-tagged truncated variants of IqgD, the CDSs of IqgD_ΔCHD (Δ53–324), IqgD_ΔGRD (Δ662–1074), and IqgD_ΔCT (Δ1292–1385) were inserted into the pDM304_N-YFP vector by ligation-independent cloning. For co-expression of YFP-IqgD and IqgD-YFP with probes for F-actin, active Rac1, and PI(3,4,5)P_3 in *D. discoideum* cells, the expression cassettes containing Lifeact-mRFP, DPAKa_GBD-mRFP, and CRAC_PH-mRFP were excised with NgoMIV from the shuttle vectors pDM330_Lifeact-mRFP [84], pDM330_DPAKa_GBD-mRFP (this work), and pDM330_CRAC_PH-mRFP [41], and ligated into the NgoMIV site of pDM304_YFP-IqgD or pDM304_IqgD-YFP. For expression of YFP-labelled probes for active Rac1 and F-actin in *D. discoideum* cells, the previously constructed pDM304_DPAKa_GBD-YFP was used [51], and oligonucleotides encoding Lifeact were hybridised and ligated into the pDM304_N-YFP vector.

The pDM1207_GFP-mRaf1_RBD [42] was used to determine macropinosome size in wild-type and *iqgD*$^{L1-}$ cells. To determine macropinosome size in IqgD-overexpressing cells, the GFP-mRaf1_RBD-containing expression cassette was cut with NgoMIV from pDM1019_mRaf1_RBD [42] and ligated into the NgoMIV site of pDM358 [83]. This vector was co-transfected with the pDM1208_IqgD vector in wild-type cells. For the pDM1208_IqgD vector, the CDS of IqgD was amplified by PCR and inserted into the pDM1208 vector [85] by ligation-independent cloning.

For the yeast two-hybrid assay, pGBKT7- and pGADT7-derived vectors were used (Matchmaker™ GAL4 Two-Hybrid System 3, Clontech). The CDS of IqgD was cloned into pGADT7 in two steps. The N-terminal half was amplified by PCR and cloned into the BglII and BamHI sites of pGADT7. The C-terminal half was then cut from the cloning vector pUC18_IqgD and ligated into the BamHI and SacI sites of pGADT7_N-IqgD. The CDS of IqgD_GRD (662–1074) was amplified by PCR and cloned into the BamHI and SacI sites of the pGADT7 vector. The CDS of IqgD was cloned into pGBKT7 in two steps. The N-terminal half was amplified by PCR and cloned into BglII and BamHI of pGBKT7. The C-terminal part was then amplified by PCR and cloned into the BamHI and SalI sites of pGBKT7_N-IqgD. The vector pGADT7-IqgC was previously constructed [41].

The tested GTPases of the Ras and Rho families were cloned into the pGBKT7 vector as ΔCAAX truncations. The pGBKT7 vectors for RasB(G15V/Q64L/S20N), RasG(G12V/Q61L/S17N), RasS(G12V/S17N), RapA(G14V/Q65E), Rac1A(G12V/Q61L/T17N), Rac1C(T17N), RacB(G12V), RacC(G15V/T20N) and RacG(G12V) were constructed previously [39, 41, 84, 86]. Rac1B(wt)_ΔCAAX was amplified by PCR from pDGFP-Rac1B(wt) [87], cloned into the BamHI and EcoRI sites of pGBKT7, and then mutated to pGBKT7_Rac1B(G12V/T17N) by site-directed mutagenesis (Q5 Site-Directed Mutagenesis Kit, NEB). To generate pGBKT7_Rac1C(G12V) and pGBKT7_RacB(Q61L/T17N), the previously constructed pGBKT7_Rac1C(T17N) and pGBKT7_RacB(G12V) were sequentially mutated by site-directed mutagenesis. To obtain pGBKT7_RacG(T17N), pGBKT7_RacG(G12V) was mutated.

For the BiFC assay in living *D. discoideum iqgD*$^{L1-}$ cells, the previously described vectors pDM304_N-VC and pDM344_N-VN were used [84]. The CDSs of full-length (FL) IqgD, IqgD_GRD (662–1074), IqgD_ΔGRD, IqgD_ΔCT and IqgD_311–1385 were inserted into pDM304_N-VC by ligation-independent cloning. The CDSs of the potential binding partners Rac1A, Rac1B and Rac1C, their respective mutant forms, as well as CI and CII, were cloned into pDM344_N-VN. To allow simultaneous expression of VC-IqgD and VN-Rac1 from the same vector, the expression cassettes encoding VN-Rac1A(wt/G12V/Q61L/T17N), VN-Rac1B(wt), and VN-Rac1C(wt/G12V/T17N) were excised with NgoMIV and ligated into the NgoMIV site of pDM304_VC-IqgD. The expression cassettes encoding VN-Rac1C(Q61L), VN-CI and VN-CII were ligated into the NgoMIV site of pDM358, and these vectors were co-transfected with pDM304 encoding the respective VC-IqgD variant. To analyse the intensity of Venus signals resulting from the interaction of IqgD and Rac1 on macropinocytic cups, the BiFC vectors pDM304_VC-IqgD_VN-Rac1A/Rac1B/Rac1C(wt) were co-transfected with pDM358_mRFP-mRaf1_RBD.

For the purification of GST-tagged FL IqgD and the truncated protein IqgD_1-575 from *Escherichia coli* cells, the CDS of IqgD was inserted into the pGEX-6P-1 vector by ligation-independent cloning and the CDS of IqgD_1-575 was amplified by PCR and ligated into the BamHI and SalI sites of pGEX-6P-1. For the GST-Rac1A pull-down assays, pGEX-5X-1_Rac1A(wt) [52], pGEX-6P-1_Rac1A(Q61L) and pGEX-6P-1_Rac1A(T17N) were used. Rac1A(Q61L) and Rac1A(T17N) were amplified by PCR from pDM344_VN-Rac1A(Q61L/T17N) and cloned into the BamHI and SalI sites of the pGEX-6P-1 vector. To construct vectors for the expression and purification of the truncated IqgD_1-592 and IqgD_311–1385 proteins from insect cells, their CDSs were amplified by PCR and inserted into the pCoofy51 vector [88] by ligation-independent cloning.

The pLPBLP_iqgD^{L1}_KO vector was constructed to generate *iqgD*$^{L1-}$ cells. The 3′ homology region of the *iqgD*^{L1} gene was amplified by PCR and cloned into the PstI and BamHI sites of the pLPBLP vector [89]. The 5′ homology region extending upstream into the promoter was synthesised (GenScript) and ligated into the SalI and HindIII sites of the same pLPBLP vector. To obtain *iqgD*$^{L1-}$ cells sensitive to blasticidin, the blasticidin resistance cassette was excised by Cre recombinase, transiently expressed from the pTX-NLS-cre vector [90]. The pLPBLP_iqgD^{L2}_KO vector was constructed to generate *iqgD*$^{L1-/L2-}$ cells. The 5′ and 3′ homology regions of the *iqgD*^{L2} gene were amplified by PCR and cloned into the SalI and HindIII, and PstI and BamHI sites of the pLPBLP vector, respectively. The pDM1490 vector containing a hygromycin resistance cassette between the 5′ and 3′ homology regions of the *rac1A* gene [85] (a gift from Dr. Arjan Kortholt, University of Groningen) was used to generate *rac1A*$^{-}$ cells.

Supporting Table S1 lists the oligonucleotides used in this work.

Cell culture

D. discoideum axenic strain AX2 was used as the parental strain to generate *iqgD*$^{-}$ and *rac1A*$^{-}$ cells. *Dgap1*$^{-}$/*gapA*$^{-}$, *ctxA*$^{-}$, *ctxB*$^{-}$, and *ctxA*$^{-}$/*ctxB*$^{-}$ cells in the AX2 background were generated previously [36, 53]. Cells were cultivated at 22 °C, either attached to cell culture dishes or shaken in suspension at 150 rpm in HL5 medium without glucose (Formedium), supplemented with 18 g/l maltose (Sigma-Aldrich), 50 µg/ml ampicillin (Sigma-Aldrich), and 40 µg/ml streptomycin (Fluka). Transfection by electroporation and clone selection were performed as previously described [90].

To analyse the growth rate in shaken suspension, 5×10^4 mid-log phase cells were inoculated into 20 ml of medium in 100 ml flasks. Cell concentration was determined daily for 5 days using a CellDrop counter (DeNovix). To analyse the growth rate in shaken suspension with bacteria, 5×10^4 mid-log phase cells were inoculated into 20 ml of an *E. coli* B/2 bacterial suspension with an optical density at 600 nm (OD_{600}) of approximately 20 in phosphate buffer in 100 ml flasks. Cells were counted daily for 2 days. To analyse growth on bacterial lawns of *Klebsiella aerogenes* or *E. coli* B/2, cells were plated with a dense suspension of bacteria on SM agar as for clonal selection. To examine the effect of bacterial lawn density on plaque size, cells were plated with undiluted bacterial suspension (OD_{600} = 4), and with 1:4 and 1:16 diluted bacterial suspensions. Plaques were imaged after 4 days on lawns of *K. aerogenes* and after 5 days on lawns of *E. coli* B/2. Plaque diameters were measured using *ImageJ* [91]. The growth of individual plaques on *K. aerogenes* lawns was recorded from the third day onwards until the plaques grew out of the field of view. To measure the speed of plaque expansion, plaques were recorded from the third day onwards every 24 h. All plaque recordings were made using a Discovery.V8 (Zeiss) stereomicroscope equipped with a Sony XC-75CE CCD camera.

Generation of *iqgD*$^{L1-}$, *iqgD*$^{L1-/L2-}$, and *rac1A*$^{-}$ cells

To generate *iqgD*$^{L1-}$ cells, wild-type AX2 cells were transfected with 35 µg of BamHI/SalI-linearised and dephosphorylated pLPBLP_iqgD^{L1}_KO vector. Transfectants were selected in HL5 medium containing 10 µg/ml blasticidin S (Sigma-Aldrich) for 14 days. After clonal selection, initial screening for *iqgD*^{L1} disruption was performed by PCR. The gDNA of potential clones was digested with ClaI and analysed by Southern blot using a bsr probe complementary to the CDS of blasticidin S

deaminase. The membrane was then stripped and rehybridised with the R probe complementary to the *iqgD* gene. Inactivation of the *iqgD*^{L1} gene (clone IW047) was also confirmed by western blot using anti-IqgD antibody. The *iqgD* gene was disrupted in the same way in AX2-214 cells newly obtained from Dr. Annette Müller-Taubenberger (Ludwig Maximilian University of Munich), and successful inactivation of the gene was confirmed by PCR and western blot.

To generate *iqgD*$^{L1-/L2-}$ cells, the bsr cassette was removed from the *iqgD*^{L1} locus. *IqgD*$^{L1-}$ cells were transfected with 35 µg of the pTX-NLS-Cre vector and cultivated in HL5 medium containing 10 µg/ml G418 for 8 days. After clonal selection on a bacterial lawn, cells sensitive to both blasticidin S and G418 were selected, and excision of the bsr cassette was confirmed by PCR. The *iqgD*$^{L1-}$ cells with the bsr cassette removed were transfected with 35 µg of BamHI/SalI-linearised and dephosphorylated pLPBLP_iqgD^{L2}_KO vector. Transfectants were selected as previously described. Disruption of *iqgD*^{L2} (clone IW052) was confirmed by PCR and sequencing.

Rac1A^{-} cells were generated by transfecting wild-type AX2 cells with 10 µg of PvuII-digested and dephosphorylated pDM1490 containing the 5′ and 3′ homology regions of the *rac1A* gene. Clones were selected in 96-well plates in HL5 medium containing 50 µg/ml hygromycin B (Sigma-Aldrich). Transfectants were diluted and plated at a density of approximately 0.3 cell/well. Initial screening for *rac1A* gene disruption was performed by PCR. The gDNA of positive clones was digested with ClaI and analysed by Southern blot using a hygr probe specific for the CDS of hygromycin phosphotransferase. The membrane was then stripped and rehybridised with the L probe complementary to the *rac1A* gene. This *rac1A*$^{-}$ clone was named IW061.

A PCR DIG Probe Synthesis Kit (Roche) was used to label DNA probes for Southern blot with digoxigenin, and the hybridised DNA bands were visualised using a DIG Luminescent Detection Kit (Roche) on the Alliance Q9 Mini Chemiluminescence Imaging System (Uvitec).

Quantitative real-time PCR

To compare the relative expression of the *iqgD* gene between wild-type and *iqgD*$^{L1-}$ cells, total RNA was extracted using the RNeasy Mini Kit (Qiagen) according to the manufacturer's instructions and reverse transcribed into cDNA using the High Capacity RNA-to-cDNA Kit (Applied Biosystems). The resulting cDNA was used as a template in qPCR with Power SYBR Green PCR Master Mix (Applied Biosystems) on the ABI 7300 Real-Time PCR system (Applied Biosystems). To quantify *iqgD* gene expression in *iqgD*$^{L1-}$ cells relative to wild-type cells, the Pfaffl method was used, which accounts for the amplification efficiency of each gene [92]. *IqgD* gene expression was normalised to the expression level of the housekeeping gene *gpdA*.

Yeast two-hybrid assay

To investigate direct protein interactions using the yeast two-hybrid assay, we used the Matchmaker GAL4 Two-Hybrid System 3 (Clontech Laboratories). The *Saccharomyces cerevisiae* strain AH109 was co-transfected with the pGBKT7- and pGADT7-derived plasmid pair. Yeast growth on selection plates lacking leucine and tryptophan (-LW) confirmed efficient co-transfection. Direct protein interactions were analysed on selection plates lacking leucine, tryptophan, and histidine (-LWH), with 0.5 mM 3-amino-1,2,4-triazole (3-AT).

Purification of GST-IqgD_1-575 and anti-IqgD antibody production

E. coli Rosetta 2 cells (Novagen) were transformed with the pGEX-6P-1-IqgD_1-575 vector, and expression of recombinant GST-tagged IqgD_1-575 protein was induced overnight with 0.75 mM isopropyl-β-D-thiogalactoside (IPTG) at 21 °C and 150 rpm. The bacteria were harvested and lysed by ultrasonication in lysis buffer (30 mM Hepes pH 7.4, 150 mM NaCl, 2 mM EDTA, 1 mM DTT, 5% glycerol, 5 mM benzamidine hydrochloride, 0.5 mM 4-(2-aminoethyl)benzenesulfonyl fluoride hydrochloride, and 2 units/ml Benzonase). The fusion protein was purified from bacterial extracts by affinity chromatography using glutathione-agarose 4B (Macherey-Nagel) following standard procedures. The GST tag was cleaved off by PreScission protease (GE Healthcare) and removed by absorption on fresh glutathione-agarose. Proteins in the flow-through were then separated by size-exclusion chromatography using a HiLoad 26/600 Superdex 200 column controlled by an Äkta Purifier System. Protein concentration was determined by absorption spectroscopy using extinction coefficients derived from the amino acid sequence. Polyclonal antibodies against IqgD were raised by immunising female New Zealand white rabbits (Charles River) with tag-free IqgD_1-575 following standard procedures.

Statement on care and use of animals

The immunisation of rabbits for the generation of polyclonal antibodies was conducted in accordance with national guidelines for the care and maintenance of laboratory animals and approved by the Hannover Medical School Institutional Animal Care Facility and the Lower Saxony State Office for Consumer Protection and Food Safety under application number 22–00236 to J.F.

Purification of recombinant IqgD_1-592 and IqgD_311-1385 from insect cells

Purification of recombinant proteins was performed at the EMBL Protein Expression and Purification Core Facility in Heidelberg, Germany. The pCoofy51 plasmids encoding the N-terminal TwinStrep-tagged IqgD_1-592 and IqgD_311–1385 were used for transposition into *E. coli* DH10EMBacY cells (Geneva Biotech). Insertion of the i*qgD* CDSs into the bacmid DNA was verified by PCR. The purified bacmid DNA was transfected into Sf9 insect cells using XtremeGENE HP (Sigma-Aldrich) DNA transfection reagent. After three days at 27 °C, YFP-positive cells were detected by fluorescence microscopy and the V0 baculoviruses were harvested. To amplify the recombinant baculoviruses, 25 ml of Sf9 cells at a density of 1×10^6 cells/ml were infected with 3 ml of V0. The Sf9 suspension cultures were incubated for 3 days at 27 °C, after which the V1 baculovirus stocks were harvested. For large-scale expression, 4 × 1 l of Sf21 suspension cultures in Sf-900 III SFM medium (Thermo Fisher Scientific) at a density of 1×10^6 cells/ml were infected with 3.3 ml of PKH V1 baculoviruses (1:300 dilution). The infected Sf21 cultures were incubated at 27 °C. After 3 days, the cultures were harvested by centrifugation (20 min, 550 × g, 4 °C) and the cell pellets were flash-frozen and stored at -80 °C. For protein purification, the cell pellets were thawed and resuspended in cold lysis buffer (50 mM Tris-HCl pH 8.0, 500 mM NaCl, 1 mM DTT, 10% glycerol, 2 mM $MgCl_2$, SmNuclease and cOmplete EDTA-free Protease Inhibitors, Roche). All subsequent purification steps were performed at 4–8 °C. Cells were lysed by 5 passages through a microfluidizer device, followed by centrifugation (30 min, 140,000 × g, 4 °C). The cleared lysate was loaded onto a 5 ml Strep-Tactin Superflow High Capacity column (IBA) preequilibrated with 50 mM Tris-HCl pH 8.0, 500 mM NaCl, 1 mM DTT and 10% glycerol. After loading, the Strep-Tactin column was washed with equilibration buffer and eluted with equilibration buffer supplemented with 5 mM Desthiobiotin. After SDS-PAGE analysis, elution fractions containing the respective IqgD proteins were pooled, concentrated to ~1 ml, and injected onto a Superdex 200 Increase 10/300 size exclusion chromatography column (Cytiva) preequilibrated with 50 mM Tris pH 8.0, 300 mM NaCl, 1 mM DTT, 2 mM $MgCl_2$ and 10% glycerol. The IqgD-containing elution fractions were pooled and concentrated to ~1–2 mg/ml. The final IqgD samples were aliquoted, flash-frozen in liquid nitrogen and stored at -80 °C until use. The identity and intactness of the purified IqgD_1-592 and IqgD_311–1385 proteins were confirmed by mass spectrometry (performed by the EMBL Proteomics Core Facility). The oligomeric state of both proteins was assessed by mass photometry using the Refeyn TwoMP instrument. Both IqgD_1-592 and IqgD_311–1385 were found to be monomeric, although for IqgD_311–1385 some additional species with higher and lower molecular weights were also observed.

Co-immunoprecipitation

For co-immunoprecipitation of actin and CI and CII with endogenous IqgD, a polyclonal anti-IqgD antibody was bound to Protein A–Sepharose CL-4B (GE Healthcare), followed by overnight incubation of the beads with lysates from wild-type and IqgD-overexpressing cells. For the negative control, a nonspecific antibody was used. After elution of the protein complexes captured by the antibody, the samples were analysed by immunoblotting using anti-actin mAb 224-236-1 [93], anti-cortexillin I mAb 241-438-1 [53], and anti-cortexillin II mAb 232-238-10 [53].

GST pull-down assays

E. coli Rosetta 2 cells (Novagen) were transformed with the pGEX-5X-1_Rac1A(wt) and pGEX-6P-1_Rac1A(Q61L/T17N) vectors, and expression of GST-Rac1A(wt/Q61L/T17N) was induced overnight with 0.25 mM IPTG at 25 °C and 150 rpm. The recombinant proteins were affinity-purified from bacterial lysate using glutathione-agarose (Thermo Scientific) according to the manufacturer's instructions. Purified GST-Rac1A(wt) protein was loaded with GDP or GTPγS as previously described [52]. To examine whether IqgD exists in a complex with Rac1A, lysates of wild-type and IqgD-overexpressing cells were incubated with immobilised GST-Rac1A(wt) for 2 h at 4 °C as previously described [51]. To test IqgD binding to mutant variants of Rac1A, cell lysates were incubated with immobilised GST-Rac1A(Q61L/T17N) overnight at 4 °C. To test direct binding of IqgD to Rac1A, 5 µg of truncated IqgD_311–1385 purified from insect cells was incubated with GDP- and GTPγS-loaded GST-Rac1A for 2 h at 4 °C. IqgD binding was analysed by immunoblotting with polyclonal anti-IqgD antibody. To investigate whether cortexilins bind to IqgD bound to Rac1A, lysate of *dgap1*$^-$*/gapA*$^-$ cells was incubated with IqgD_311–1385 bound to GST-Rac1A overnight at 4 °C. Cortexillin binding was analysed by immunoblotting with anti-CI mAb 241-438-1 [53] and anti-CII mAb 232-238-10 [53]. The lysis buffer used in pull-down assays contained: 30 mM Tris-HCl pH 7.5, 40 mM NaCl, 1 mM EGTA pH 7.3, 2 mM DTT, 5 mM $MgCl_2$, 0.5% n-octylpolyoxyethylene, 1 mM PMSF, 5 mM benzamidine, and cOmplete EDTA-free Protease Inhibitors Cocktail (Roche). In all pull-down assays, GST pull-down was used as a negative control.

GAP assay

The GAP assay was performed using the GTPase-Glo Assay Kit (Promega) according to the manufacturer's

protocol for 384-well plates. The GTPase activity of 2 µM human Rac1(wt) (ab89246, Abcam) was measured in the absence and presence of purified IqgD_311–1385 (2 µM and 4 µM) in GAP buffer containing 5 µM GTP. Luminescence was measured using a Spark multimode plate reader (Tecan).

Actin co-sedimentation assay

Ca^{2+}-ATP G-actin was purified from rabbit skeletal muscle as previously described [94] and stored on ice in G-buffer (5 mM Tris-HCl pH 8.0, 0.2 mM $CaCl_2$, 0.5 mM DTT, 0.2 mM ATP). IqgD_1-575 and IqgD_1-592 were purified from bacterial and insect cells, respectively, as described above. For co-sedimentation assays, IqgD_1-575 and IqgD_1-592 were clarified by centrifugation at 150,000 × g for 45 min at 4 °C using an Optima MAX-XP ultracentrifuge (Beckman Coulter). Next, 30 µM or 4 µM G-actin was polymerised for 2 h at room temperature in the absence or presence of 4 µM IqgD_1-592 or 4 µM IqgD_1-575 in actin polymerisation buffer (10 mM imidazole pH 7.0, 2 mM $MgCl_2$, 50 mM KCl, 1 mM ATP). For high-speed co-sedimentation assays, samples were centrifuged under the same conditions as above. For low-speed co-sedimentation assays, samples were centrifuged at 17,000 × g for 30 min at 4 °C in a PICO17 centrifuge (Heraeus). The supernatants were carefully separated from the pellets and adjusted to the same volume with SDS sample buffer. Proteins were resolved by SDS-PAGE and visualised by Coomassie Blue staining. Protein content in pellet and supernatant fractions was determined by densitometry.

F-/G-actin ratio

To determine the F-/G-actin ratio, a previously described protocol was adapted [95]. Cells grown overnight in shaken suspension to mid-log phase were collected at 2 × 10^7 cells, washed in cold wash buffer (10 mM Tris-HCl pH 7.5, 50 mM KCl, 1 mM EGTA, 5 mM $MgCl_2$, 0.5 mM DTT, 1 mM PMSF, 1 mM ATP), and lysed with 600 µl cold lysis buffer (wash buffer containing 5% glycerol, 1% Nonidet P-40, and cOmplete EDTA-free Protease Inhibitors, Roche). A 200 µl aliquot of lysate was collected to measure protein concentration. The remaining 400 µl of lysate was used to separate F- and G-actin by centrifugation in low-protein-binding tubes (LoBind Tubes, Eppendorf). Lysate was centrifuged at 30,000 × g for 2 h at 4 °C. The supernatant was collected, and the pellet was resuspended in 400 µl lysis buffer. The F-actin fraction was sonicated three times for 30 s at an amplitude of 60 (Ultrasonic Processor, Cole-Parmer). One microgram of protein from each fraction was separated by SDS-PAGE and immunoblotted with anti-actin mAb 224-236-1 [93]. The detected bands were analysed by densitometry using *ImageJ* [91].

Phagocytosis

A clearance assay was used to measure phagocytosis of bacteria from suspension [84]. Mid-log phase cells grown overnight in shaken suspension were washed with ice-cold phosphate buffer, adjusted to a concentration of 2 × 10^6 cells/ml in 10 ml phosphate buffer, and shaken for 30 min at 150 rpm. An equal volume of *E. coli* DH5α or B/2 suspension with an optical density at 600 nm (OD_{600}) of approximately 1.4 in phosphate buffer was added to the cells. Immediately and every hour for 6 hours, 1.2 ml samples were withdrawn, supplemented with Na-azide to a final concentration of 15 mM, and vortexed for 1 min to remove surface-bound bacteria. After pelleting the cells by centrifugation for 1 min at 700 × g, the OD_{600} of the supernatant containing bacteria was measured. All experiments were corrected for protein content and normalised to the initial OD_{600} of wild-type cells. Quantitative analysis of yeast particle phagocytosis was performed as previously described [41]. Cells were grown to mid-log phase in shaken suspension, and their density was adjusted to 2 × 10^6 /ml in 8 ml. A 400 µl aliquot was taken to determine protein content. At zero time, a six-fold higher concentration of TRITC-labelled yeast particles was added to the cell suspension, and 500 µl aliquots were collected at each time point, starting immediately. Cells were mixed with 50 µl ice-cold Trypan Blue solution (4 mg/ml; Sigma-Aldrich), briefly vortexed, and shaken at 500 rpm for 3 min at 4 °C, protected from light. After centrifugation at 800 × g for 2 min at 4 °C, the cell pellets were washed with 1 ml ice-cold phosphate buffer and resuspended in 500 µl ice-cold phosphate buffer. Fluorescence was measured immediately in triplicate in a microtiter plate using a Spark multimode plate reader (Tecan), with excitation and emission wavelengths set at 545 nm and 575 nm, respectively. Relative fluorescence was normalised to protein content, determined using Roti®-Quant (Roth) Bradford solution.

Cell-substrate adhesion

To assess cell-substrate adhesion, cell detachment experiments were performed as previously described [86]. Subconfluent cells were plated on a 6 cm Petri dish in HL5 medium without selection antibiotics at a concentration of 1 × 10^5 cells/ml one day before the experiment. The next day, plates were shaken on an orbital shaker in fresh HL5 medium. Detached and attached cells were collected, and cell concentration was measured with a CellDrop counter (DeNovix) for both attached and detached cells before shaking (0 min), and at 30 min and 60 min after shaking at 100 rpm at 22 °C. Results are presented as the percentage of detached cells out of the total number of cells.

Fluorescence microscopy

Confocal microscopy was performed using a Leica TCS SP8 X laser scanning confocal microscope equipped with an HC PL APO CS2 63×/1.4 oil objective, a 405 nm diode laser, and a supercontinuum excitation laser (Leica Microsystems). Images were acquired using Leica Application Suite X software. To examine the (co)localisation of YFP- and mRFP-tagged proteins, phagocytosis of TRITC-labelled yeast particles, and BiFC signal in living *D. discoideum*, the excitation wavelengths and detection ranges used were as follows: 511 nm and 520–565 nm for YFP, 515 nm and 525–600 nm for Venus, 565 nm and 575–650 nm for TRITC, and 585 nm and 592–650 nm for mRFP. Cells were imaged in LoFlow medium for BiFC experiments and in HL5 medium for other experiments. The ambient temperature was lowered to stabilise the temperature at the microscope slide at 22 °C. To assess cytokinesis efficiency of cells from the vegetative zone of a spreading plaque, cells were harvested with an inoculation loop, washed free of bacteria in phosphate buffer, fixed with 2% paraformaldehyde (Sigma-Aldrich), and stained with 1 µg/ml DAPI for 30 min. The excitation wavelength and detection range for DAPI imaging were 405 nm and 430–520 nm. For immunostaining F-actin, CI, and CII, cells were fixed with cold methanol for 5 min at -20 °C and then stained with anti-actin mAb 224-236-1 [93], anti-cortexillin I mAb 241-438-1 [53], or anti-cortexillin II mAb 232-238-10 [53], respectively. Alexa 633-conjugated goat anti-mouse IgG (Cell Signaling) was used as the secondary antibody. To estimate fluid uptake, cells were incubated in the dark in HL5 medium containing 2 mg/ml TRITC-dextran. After 10 min, cells were washed twice with phosphate buffer and immediately imaged. Each cell was outlined, and TRITC fluorescence within the outlined area was measured in *ImageJ* [91]. Macropinocytosis was expressed as the ratio of TRITC intensity to cell area [96]. To measure fluorescence intensity profiles of YFP-IqgD_FL, YFP-IqgD_ΔGRD, and YFP-IqgD_ΔCT along the cell cortex, cell outlines and cortical fluorescence profiles were extracted using QuimP in *ImageJ* [91, 97]. Cortical fluorescence intensities were normalised to the mean fluorescence intensity of the cell interior. The resulting QuimP output was further analysed in MATLAB using a custom script. Fluorescence profiles were interpolated onto a common normalised cortical coordinate, and profiles from mutant cells were circularly shifted relative to the full-length construct to align cortical features. Aligned profiles were smoothed using a circular smoothing spline, and macropinocytic cup regions were manually annotated based on the cortical fluorescence profile and displayed as distinct line segments. To determine the efficiency of phagocytosis of surface-bound microbeads, a previously described protocol was adapted [46]. Glass coverslips were incubated for 30 min in poly-L-lysine (0.01%, Sigma-Aldrich). After washing the coverslips three times with water, a suspension of 3.6×10^8 1 µm microbeads (Fluoresbrite® YG Microspheres, Polysciences) in 350 µl phosphate buffer was added to the coverslips. After 20 min of incubation, an equal volume of 9% glutaraldehyde (Sigma-Aldrich) in phosphate buffer was added to the microbead solution. Following 20 min of incubation and washing the coverslips five times with water, 5 mg/ml sodium borohydride (Sigma-Aldrich) was added and incubated for 5 min to quench the glutaraldehyde. After washing the coverslips five times with phosphate buffer, a suspension of cells was added to the coverslips and incubated for 30 min at 22 °C. Cells were then fixed with cold methanol for 5 min at -20 °C. The next day, cells were imaged in *xyz* mode and analysed in 3D to determine how many microbeads they had ingested. The excitation wavelength and detection range for microbeads were 458 nm and 469–495 nm, respectively. For the latrunculin assay, Latrunculin A (Sigma-Aldrich) at a final concentration of 5 µM was added to YFP-IqgD-expressing cells, which were imaged at the indicated times. After 20 min, cells were washed with phosphate buffer and further imaged. To analyse macropinosome size, live cells expressing the GFP-mRaf1_RBD probe in HL5 medium at 22 °C were imaged in *xyzt* mode using a Dragonfly spinning disc confocal microscope (Andor, Oxford Instruments) with a 100×/1.45 oil objective (Nikon), a Sona 4.2B-6 (sCMOS) camera (Andor, Oxford Instruments), and Fusion acquisition software. The excitation wavelength was 488 nm, and the detection bandpass filter 521/38 was used. For (co)localisations of GFP-/YFP- and mRFP-tagged proteins, live cells were imaged in *xyt* mode, with excitation wavelengths 488 nm, 514 nm and 561 nm, and detection bandpass filters 521/38, 571/78 and 594/43 for GFP, YFP and mRFP, respectively. Macropinosome size was determined by measuring the length of the major axis upon macropinosome closure using *ImageJ* [91]. To analyse random migration, cells were plated at low density in HL5 medium on a 35 mm glass-bottom dish (MatTek) 1 h before the experiment. Cells were imaged at 22 °C every 10 s for 1 h using a dark-field microscope (Axiovert 135, Zeiss) with a 5×/0.15 objective [98], an X-Cite 120Q (EXFO) lamp, a pco.panda 4.2 sCMOS (PCO) camera, and Micro-Manager 2.0 acquisition software [99]. Acquired images were processed in *ImageJ* [91], and single-cell trajectories were detected using the *ImageJ* plugin *TrackMate* [100, 101]. Trajectory data were imported into Microsoft Excel with integrated DiPer macros, which were used to calculate cell speed and directional persistence [102]. To assess the localisation of IqgD at ventral actin dots on the substrate, $iqgD^{L1-}$ cells co-expressing YFP-IqgD and Lifeact-mRFP were seeded in HL5 medium onto 35 mm glass-bottom dishes (Ibidi) at

least 1 h before imaging. Time-lapse TIRF imaging was performed using an Eclipse TI-E inverted microscope (Nikon) equipped with a TIRF Apo 100×/1.45 objective and an iXon3 897 EMCCD camera (Andor). Images were recorded at 5 s intervals for at least 5 min using the 488-nm and 561-nm laser lines.

Statistical analysis

The statistical test used for each experiment is indicated in the corresponding figure legend. All statistical analyses were performed using GraphPad Prism 5.

Abbreviations

ABD	Actin binding domain
Arp2/3	Actin related protein 2/3 complex
Arp3	Actin related protein 3
BiFC	Bimolecular fluorescence complementation
bsr	Blasticidin resistance cassette
CBB	Coomassie Brilliant Blue
Cdc42	Cell division control protein 42
CHD	Calponin homology domain
CHf1/2	Calponin homology fimbrin-type domain 1/2
CI/II	Cortexillin I/II
CT	C-terminal domain
DGAP1	GTPase-activating protein 1
Dia1	Diaphanous-related formin 1
DPAKa	*Dictyostelium* p21-activated kinase A
GAP	GTPase-activating protein
GAPA	GTPase-activating protein A
GBD	GTPase-binding domain
GRD	GAP-related domain
hygr	Hygromycin resistance cassette
IQ	Isoleucine–glutamine motif
IQGAP	IQ motif-containing GTPase-activating protein
N-WASP	Neural Wiskott–Aldrich syndrome protein
PAR	Phagocytic adhesion ring
$PI(3,4,5)P_3$	Phosphatidylinositol (3,4,5)-trisphosphate
RasGAP	Ras GTPase-activating protein
RGCT	RasGAP C-terminal domain
Scar/WAVE	Suppressor of cAR/WASP-family verprolin homologous protein
TIRF	Total internal reflection fluorescence
VC	Venus C-terminal fragment
VN	Venus N-terminal fragment
WASP	Wiskott–Aldrich syndrome protein
WW	Tryptophan-containing proline-rich motif-binding region
YFP	Yellow fluorescent protein

Supplementary Information

The online version contains supplementary material available at https://doi.org/10.1186/s12964-026-03074-w.

Supplementary Material 1.

Acknowledgements

The authors thank Dr. Annette Müller-Taubenberger (Ludwig Maximilian University of Munich, Germany) for providing AX2-214 cells and Dr. Arjan Kortholt (University of Groningen, Netherlands) for the pDM1490 vector used to generate the *rac1A*$^-$ knockout.

Authors' contributions

V.F. designed research. All authors performed research. A.Č., D.P., M.Š., J.S., L.H., M.M.[3] , and V.F. analysed data. V.F. wrote the paper with contributions from other authors. All authors read and approved the final manuscript.

Funding

This work has been supported by the Croatian Science Foundation under the project IP-2020-02-1572 to V.F.

Data availability

All data generated or analysed during this study are included in this published article and its supplementary information files. All materials are available from the corresponding author upon reasonable request.

Declarations

Ethics approval and consent to participate

Not applicable.

Consent for publication

Not applicable.

Competing interests

The authors declare no competing interests.

Author details

[1]Division of Molecular Biology, Ruđer Bošković Institute, Bijenička cesta 54, Zagreb 10000, Croatia
[2]Institute for Biophysical Chemistry, Hannover Medical School, Hannover 30625, Germany
[3]Division of Organic Chemistry and Biochemistry, Ruđer Bošković Institute, Zagreb 10000, Croatia

Received: 2 March 2026 / Accepted: 11 July 2026
Published online: 16 July 2026

References

1. Hedman AC, Smith JM, Sacks DB. The biology of IQGAP proteins: beyond the cytoskeleton. EMBO Rep. 2015;16(4):427–46. https://doi.org/10.15252/embr.201439834 . PubMed PMID: 25722290; PubMed Central PMCID: PMC4388610.
2. Mosaddeghzadeh N, Pudewell S, Bazgir F, Kazemein Jasemi NS, Krumbach OHF, Gremer L, et al. CDC42-IQGAP Interactions Scrutinized: New Insights into the Binding Properties of the GAP-Related Domain. Int J Mol Sci. 2022;23(16):8842. https://doi.org/10.3390/ijms23168842 . PubMed PMID: 36012107; PubMed Central PMCID: PMC9408373.
3. Ren JG, Li Z, Sacks DB. IQGAP1 modulates activation of B-Raf. Proc Natl Acad Sci U S A. 2007;104(25):10465–9. https://doi.org/10.1073/pnas.0611308104 . PubMed PMID: 17563371; PubMed Central PMCID: PMC1965536.
4. Roy M, Li Z, Sacks DB. IQGAP1 Binds ERK2 and Modulates Its Activity. J Biol Chem. 2004;279(17):17329–37. 10.1074. /jbc.M308405200 PubMed PMID: 14970219.
5. Roy M, Li Z, Sacks DB. IQGAP1 is a scaffold for mitogen-activated protein kinase signaling. Mol Cell Biol. 2005;25(18):7940–52. https://doi.org/10.1128/MCB.25.18.7940-7952. 2005 PubMed PMID: 16135787; PubMed Central PMCID: PMC1234344.
6. Bardwell AJ, Lagunes L, Zebarjedi R, Bardwell L. The WW domain of the scaffolding protein IQGAP1 is neither necessary nor sufficient for binding to the MAPKs ERK1 and ERK2. J Biol Chem. 2017;292(21):8750–61. https://doi.org/10.1074/jbc.M116.767087 . PubMed PMID: 28396345; PubMed Central PMCID: PMC5448102.
7. Choi S, Hedman AC, Sayedyahossein S, Thapa N, Sacks DB, Anderson RA. Agonist-stimulated phosphatidylinositol-3,4,5-trisphosphate generation by scaffolded phosphoinositide kinases. Nat Cell Biol. 2016;18(12):1324–35. https://doi.org/10.1038/ncb3441 . PubMed PMID: 27870828; PubMed Central PMCID: PMC5679705.
8. Thines L, Roushar FJ, Hedman AC, Sacks DB. The IQGAP scaffolds: Critical nodes bridging receptor activation to cellular signaling. J Cell Biol. 2023;222(6):e202205062. https://doi.org/10.1083/jcb.202205062.
9. Watanabe T, Wang S, Kaibuchi K. IQGAPs as Key Regulators of Actin-cytoskeleton Dynamics. Cell Struct Funct. 2015;40(2):69–77. https://doi.org/10.1247/csf.15003.
10. Kurella VB, Richard JM, Parke CL, LeCour LF, Bellamy HD, Worthylake DK. Crystal Structure of the GTPase-activating Protein-related Domain from IQGAP1. J Biol Chem. 2009;284(22):14857–65.

11. Scheffzek K, Ahmadian MR, Kabsch W, Wiesmüller L, Lautwein A, Schmitz F, et al. The Ras-RasGAP complex: structural basis for GTPase activation and its loss in oncogenic Ras mutants. Science. 1997;277(5324):333–8. https://doi.org/10.1126/science.277.5324.333 . PubMed PMID: 9219684.
12. van Dam TJP, Bos JL, Snel B. Evolution of the Ras-like small GTPases and their regulators. Small GTPases. 2011;2(1):4–16. https://doi.org/10.4161/sgtp.2..1.15113 PubMed PMID: 21686276; PubMed Central PMCID: PMC3116619.
13. Morgan CJ, Hedman AC, Li Z, Sacks DB. Endogenous IQGAP1 and IQGAP3 do not functionally interact with Ras. Sci Rep. 2019;9(1):11057. https://doi.org/10.1038/s41598-019-46677-9 . PubMed PMID: 31363101; PubMed Central PMCID: PMC6667474.
14. Brill S, Li S, Lyman CW, Church DM, Wasmuth JJ, Weissbach L, et al. The Ras GTPase-activating-protein-related human protein IQGAP2 harbors a potential actin binding domain and interacts with calmodulin and Rho family GTPases. Mol Cell Biol. 1996;16(9):4869–78. PubMed PMID: 8756646; PubMed Central PMCID: PMC231489.
15. Hart MJ, Callow MG, Souza B, Polakis P. IQGAP1, a calmodulin-binding protein with a rasGAP-related domain, is a potential effector for cdc42Hs. EMBO J. 1996;15(12):2997–3005. PubMed PMID: 8670801; PubMed Central PMCID: PMC450241.
16. Ho YD, Joyal JL, Li Z, Sacks DB. IQGAP1 integrates Ca2+/calmodulin and Cdc42 signaling. J Biol Chem. 1999;274(1):464–70. https://doi.org/10.1074/jbc.274.1. .464 PubMed PMID: 9867866.
17. Kuroda S, Fukata M, Kobayashi K, Nakafuku M, Nomura N, Iwamatsu A, et al. Identification of IQGAP as a putative target for the small GTPases, Cdc42 and Rac1. J Biol Chem. 1996;271(38):23363–7. https://doi.org/10.1074/jbc.271.38.23363 . PubMed PMID: 8798539.
18. McCallum SJ, Wu WJ, Cerione RA. Identification of a putative effector for Cdc42Hs with high sequence similarity to the RasGAP-related protein IQGAP1 and a Cdc42Hs binding partner with similarity to IQGAP2. J Biol Chem. 1996;271(36):21732–7. https://doi.org/10.1074/jbc.271.36.21732 . PubMed PMID: 8702968.
19. Mataraza JM, Briggs MW, Li Z, Frank R, Sacks DB. Identification and characterization of the Cdc42-binding site of IQGAP1. Biochem Biophys Res Commun. 2003;305(2):315–21. https://doi.org/10.1016/s0006-291x. (03)00759-9 PubMed PMID: 12745076.
20. Sokol SY, Li Z, Sacks DB. The effect of IQGAP1 on Xenopus embryonic ectoderm requires Cdc42. J Biol Chem. 2001;276(51):48425–30. 10.1074. /jbc.M107975200 PubMed PMID: 11584017.
21. Swart-Mataraza JM, Li Z, Sacks DB. IQGAP1 Is a Component of Cdc42 Signaling to the Cytoskeleton. J Biol Chem. 2002;277(27):24753–63. https://doi.org/10.1074/jbc. M111165200 PubMed PMID: 11948177.
22. Nouri K, Fansa EK, Amin E, Dvorsky R, Gremer L, Willbold D, et al. IQGAP1 Interaction with RHO Family Proteins Revisited: Kinetic and equilibrium evidence for multiple distinct binding sites. J Biol Chem. 2016;291(51):26364–76. https://doi.org/10.1074/jbc.M116.752121 . PubMed PMID: 27815503; PubMed Central PMCID: PMC5159498.
23. Nouri K, Timson DJ, Ahmadian MR. New model for the interaction of IQGAP1 with CDC42 and RAC1. Small GTPases. 2020;11(1):16–22. https://doi.org/10.1080/21541248.2017.1321169 . PubMed PMID: 28622072; PubMed Central PMCID: PMC6959280.
24. Zhang B, Wang ZX, Zheng Y. Characterization of the interactions between the small GTPase Cdc42 and its GTPase-activating proteins and putative effectors. Comparison of kinetic properties of Cdc42 binding to the Cdc42-interactive domains. J Biol Chem. 1997;272(35):21999–2007. PubMed PMID: 9268338.
25. Bashour AM, Fullerton AT, Hart MJ, Bloom GS. IQGAP1, a Rac- and Cdc42-binding protein, directly binds and cross-links microfilaments. J Cell Biol. 1997;137(7):1555–66. PubMed PMID: 9199170; PubMed Central PMCID: PMC2137827.
26. Fukata M, Kuroda S, Fujii K, Nakamura T, Shoji I, Matsuura Y, et al. Regulation of Cross-linking of Actin Filament by IQGAP1, a Target for Cdc42. J Biol Chem. 1997;272(47):29579–83. https://doi.org/10.1074/jbc.272.47.29579 . PubMed PMID: 9368021.
27. Hoeprich GJ, Sinclair AN, Shekhar S, Goode BL. Single-molecule imaging of IQGAP1 regulating actin filament dynamics. Mol Biol Cell. 2022;33(1):ar2. https://doi.org/10.1091/mbc.E. 21-04-0211 PubMed PMID: 34731043; PubMed Central PMCID: PMC8886817.
28. Pelikan-Conchaudron A, Le Clainche C, Didry D, Carlier MF. The IQGAP1 protein is a calmodulin-regulated barbed end capper of actin filaments: possible implications in its function in cell migration. J Biol Chem. 2011;286(40):35119–28. https://doi.org/10.1074/jbc.M111.258772 . PubMed PMID: 21730051; PubMed Central PMCID: PMC3186398.
29. Abel AM, Schuldt KM, Rajasekaran K, Hwang D, Riese MJ, Rao S, et al. IQGAP1: insights into the function of a molecular puppeteer. Mol Immunol. 2015;65(2):336–49. https://doi.org/10.1016/j.molimm.2015.02. .012 PubMed PMID: 25733387; PubMed Central PMCID: PMC4480615.
30. Benseñor LB, Kan HM, Wang N, Wallrabe H, Davidson LA, Cai Y, et al. IQGAP1 regulates cell motility by linking growth factor signaling to actin assembly. J Cell Sci. 2007;120(4):658–69. https://doi.org/10.1242/jcs.03376 . PubMed PMID: 17264147.
31. Le Clainche C, Schlaepfer D, Ferrari A, Klingauf M, Grohmanova K, Veligodskiy A, et al. IQGAP1 stimulates actin assembly through the N-WASP-Arp2/3 pathway. J Biol Chem. 2007;282(1):426–35. 10.1074. /jbc.M607711200 PubMed PMID: 17085436.
32. Bombardier JP, Eskin JA, Jaiswal R, Corrêa IR, Xu MQ, Goode BL, et al. Single-molecule visualization of a formin-capping protein 'decision complex' at the actin filament barbed end. Nat Commun. 2015;6(1):8707. https://doi.org/10.1038/ncomms9707.
33. Pimm ML, Haarer BK, Nobles AD, Haney LM, Marcin AG, Alcaide Eligio M, et al. Coordination of actin plus-end dynamics by IQGAP1, formin, and capping protein. J Cell Biol. 2024;223(9):e202305065. https://doi.org/10.1083/jcb.202305065 . PubMed PMID: 38787349; PubMed Central PMCID: PMC11117073.
34. Smith JM, Hedman AC, Sacks DB. IQGAPs choreograph cellular signaling from the membrane to the nucleus. Trends Cell Biol. 2015;25(3):171–84. https://doi.org/10.1016/j.tcb. .2014.12.005 PubMed PMID: 25618329; PubMed Central PMCID: PMC4344846.
35. Filić V, Weber I. Queue Gaps Among the IQGAPs in Dictyostelium discoideum. Int J Mol Sci. 2026;27(12). https://doi.org/10.3390/ijms27125462.
36. Faix J, Weber I, Mintert U, Köhler J, Lottspeich F, Marriott G. Recruitment of cortexillin into the cleavage furrow is controlled by Rac1 and IQGAP-related proteins. EMBO J. 2001;20(14):3705–15. https://doi.org/10.1093/emboj/20.14.3705 . PubMed PMID: 11447112; PubMed Central PMCID: PMC125549.
37. Vlahou G, Rivero F. Rho GTPase signaling in Dictyostelium discoideum: Insights from the genome. Eur J Cell Biol. 2006;85(9–10):947–59. https://doi.org/10.1016/j.ejcb.2006.04.011.
38. Filić V, Mijanović L, Putar D, Talajić A, Četković H, Weber I. Regulation of the Actin Cytoskeleton via Rho GTPase Signalling in Dictyostelium and Mammalian Cells: A Parallel Slalom. Cells. 2021;10(7):7. https://doi.org/10.3390/cells10071592.
39. Filić V, Marinović M, Faix J, Weber I. A dual role for Rac1 GTPases in the regulation of cell motility. J Cell Sci. 2012;125(Pt 2):387–98. https://doi.org/10.1242/jcs.089680 . PubMed PMID: 22302991.
40. Lee S, Shen Z, Robinson DN, Briggs S, Firtel RA. Involvement of the cytoskeleton in controlling leading-edge function during chemotaxis. Mol Biol Cell. 2010;21(11):1810–24. https://doi.org/10.1091/mbc.E10-01-0009 . PubMed PMID: 20375144; PubMed Central PMCID: PMC2877640.
41. Marinović M, Mijanović L, Šoštar M, Vizovišek M, Junemann A, Fonović M et al. IQGAP-related protein IqgC suppresses Ras signaling during large-scale endocytosis. Proc Natl Acad Sci USA. 2019 22;116(4):1289–98. https://doi.org/10.1073/pnas.1810268116 PubMed PMID: 30622175; PubMed Central PMCID: PMC6347711.
42. Putar D, Čizmar A, Chao X, Šimić M, Šoštar M, Ćutić T, et al. IqgC is a potent regulator of macropinocytosis in the presence of NF1 and its loading to macropinosomes is dependent on RasG. Open Biol. 2024;14(1):230372. https://doi.org/10.1098/rsob.230372 . PubMed PMID: 38263885; PubMed Central PMCID: PMC10806400.
43. Filić V, Putar D, Mijanović L, Weber I. Actin dynamics controlled by IqgC, a RasGAP at the crossroads between the IQGAP and fungal GAP1 families. FEBS Open Bio. 2026;16(2):268–78. https://doi.org/10.1002/2211-5463.70083 . PubMed PMID: 40643061.
44. Jones P, Binns D, Chang HY, Fraser M, Li W, McAnulla C, et al. InterProScan 5: genome-scale protein function classification. Bioinformatics. 2014;30(9):1236–40. https://doi.org/10.1093/bioinformatics/btu031.
45. Abramson J, Adler J, Dunger J, Evans R, Green T, Pritzel A, et al. Accurate structure prediction of biomolecular interactions with AlphaFold 3. Nature. 2024;630(8016):493–500. https://doi.org/10.1038/s41586-024-07487-w.
46. Kundu S, Pal K, Pyne A, Wang X. Force-bearing phagocytic adhesion rings mediate the phagocytosis of surface-bound particles. Nat Commun. 2025;16(1):984. https://doi.org/10.1038/s41467-025-56404-w.
47. Riedl J, Crevenna AH, Kessenbrock K, Yu JH, Neukirchen D, Bista M, et al. Lifeact: a versatile marker to visualize F-actin. Nat Methods. 2008;5(7):605–7. https://doi.org/10.1038/nmeth.1220 . PubMed PMID: 18536722; PubMed Central PMCID: PMC2814344.

48. Glöckner G, Eichinger L, Szafranski K, Pachebat JA, Bankier AT, Dear PH, et al. Sequence and analysis of chromosome 2 of Dictyostelium discoideum. Nature. 2002;418(6893):79–85. https://doi.org/10.1038/nature00847 . PubMed PMID: 12097910.
49. Eichinger L, Pachebat JA, Glöckner G, Rajandream MA, Sucgang R, Berriman M, et al. The genome of the social amoeba Dictyostelium discoideum. Nature. 2005;435(7038):43–57. https://doi.org/10.1038/nature03481 . PubMed PMID: 15875012; PubMed Central PMCID: PMC1352341.
50. Bloomfield G, Tanaka Y, Skelton J, Ivens A, Kay RR. Widespread duplications in the genomes of laboratory stocks of Dictyostelium discoideum. Genome Biol. 2008;9(4):R75. https://doi.org/10.1186/gb-2008-9-4-r75 . PubMed PMID: 18430225; PubMed Central PMCID: PMC2643946.
51. Marinović M, Šoštar M, Filić V, Antolović V, Weber I. Quantitative imaging of Rac1 activity in Dictyostelium cells with a fluorescently labelled GTPase-binding domain from DPAKa kinase. Histochem Cell Biol. 2016;146(3):267–79. https://doi.org/10.1007/s00418-016-1440-9 . PubMed PMID: 27126594.
52. Faix J, Clougherty C, Konzok A, Mintert U, Murphy J, Albrecht R, et al. The IQGAP-related protein DGAP1 interacts with Rac and is involved in the modulation of the F-actin cytoskeleton and control of cell motility. J Cell Sci. 1998;111(Pt 20):3059–71. PubMed PMID: 9739079.
53. Faix J, Steinmetz M, Boves H, Kammerer RA, Lottspeich F, Mintert U, et al. Cortexillins, major determinants of cell shape and size, are actin-bundling proteins with a parallel coiled-coil tail. Cell. 1996;86(4):631–42. PubMed PMID: 8752217.
54. Santhanam B, Cai H, Devreotes PN, Shaulsky G, Katoh-Kurasawa M. The GATA transcription factor GtaC regulates early developmental gene expression dynamics in Dictyostelium. Nat Commun. 2015;6:7551. https://doi.org/10.1038/ncomms8551 . PubMed PMID: 26144553; PubMed Central PMCID: PMC4506546.
55. Stajdohar M, Rosengarten RD, Kokosar J, Jeran L, Blenkus D, Shaulsky G, et al. dictyExpress: a web-based platform for sequence data management and analytics in Dictyostelium and beyond. BMC Bioinformatics. 2017;18(1):291. https://doi.org/10.1186/s12859-017-1706-9.
56. Korenbaum E, Rivero F. Calponin homology domains at a glance. J Cell Sci. 2002;115(18):3543–5. https://doi.org/10.1242/jcs.00003 . PubMed PMID: 12186940.
57. Pikzack C, Prassler J, Furukawa R, Fechheimer M, Rivero F. Role of calcium-dependent actin-bundling proteins: characterization of Dictyostelium mutants lacking fimbrin and the 34-kilodalton protein. Cell Motil Cytoskeleton. 2005;62(4):210–31. https://doi.org/10.1002/cm.20098 . PubMed PMID: 16265631.
58. Kovar DR, Staiger CJ, Weaver EA, McCurdy DW. AtFim1 is an actin filament crosslinking protein from Arabidopsis thaliana. Plant J. 2000;24(5):625–36. https://doi.org/10.1046/j.1365-313x.2000. 00907.x PubMed PMID: 11123801.
59. Lebart MC, Hubert F, Boiteau C, Ventéo S, Roustan C, Benyamin Y. Biochemical characterization of the L-plastin-actin interaction shows a resemblance with that of alpha-actinin and allows a distinction to be made between the two actin-binding domains of the molecule. Biochemistry. 2004;43(9):2428–37. https://doi.org/10.1021/bi030151p . PubMed PMID: 14992580.
60. Mateer SC, Morris LE, Cromer DA, Benseñor LB, Bloom GS. Actin filament binding by a monomeric IQGAP1 fragment with a single calponin homology domain. Cell Motil Cytoskeleton. 2004;58(4):231–41. https://doi.org/10.1002/cm.20013 . PubMed PMID: 15236354.
61. Prassler J, Stocker S, Marriott G, Heidecker M, Kellermann J, Gerisch G. Interaction of a Dictyostelium member of the plastin/fimbrin family with actin filaments and actin-myosin complexes. Mol Biol Cell. 1997;8(1):83–95. https://doi.org/10.1091/mbc.8.1.83 . PubMed PMID: 9017597; PubMed Central PMCID: PMC276061.
62. Schwebach CL, Agrawal R, Lindert S, Kudryashova E, Kudryashov DS. The Roles of Actin-Binding Domains 1 and 2 in the Calcium-Dependent Regulation of Actin Filament Bundling by Human Plastins. J Mol Biol. 2017;429(16):2490–508. https://doi.org/10.1016/j.jmb.2017.06.021 . PubMed PMID: 28694070.
63. Nakano K, Satoh K, Morimatsu A, Ohnuma M, Mabuchi I. Interactions among a fimbrin, a capping protein, and an actin-depolymerizing factor in organization of the fission yeast actin cytoskeleton. Mol Biol Cell. 2001;12(11):3515–26. https://doi.org/10.1091/mbc.12.11.3515 . PubMed PMID: 11694585; PubMed Central PMCID: PMC60272.
64. Schwebach CL, Kudryashova E, Agrawal R, Zheng W, Egelman EH, Kudryashov DS. Allosteric regulation controls actin-bundling properties of human plastins. Nat Struct Mol Biol. 2022;29(6):519–28. https://doi.org/10.1038/s41594-022-00771-1 . PubMed PMID: 35589838; PubMed Central PMCID: PMC9358775.
65. Bush J, Franek K, Cardelli J. Cloning and characterization of seven novel Dictyostelium discoideum rac-related genes belonging to the rho family of GTPases. Gene. 1993;136(1–2):61–8. PubMed PMID: 8294042.
66. King JS, Veltman DM, Georgiou M, Baum B, Insall RH. SCAR/WAVE is activated at mitosis and drives myosin-independent cytokinesis. J Cell Sci. 2010;123(Pt 13):2246–55. https://doi.org/10.1242/jcs.063735 . PubMed PMID: 20530573; PubMed Central PMCID: PMC2886745.
67. Chung CY, Funamoto S, Firtel RA. Signaling pathways controlling cell polarity and chemotaxis. Trends Biochem Sci. 2001;26(9):557–66. https://doi.org/10.1016/S0968-0004(. 01)01934-X PubMed PMID: 11551793.
68. Mosaddeghzadeh N, Nouri K, Krumbach OHF, Amin E, Dvorsky R, Ahmadian MR. Selectivity Determinants of RHO GTPase Binding to IQGAPs. Int J Mol Sci. 2021;22(22):12596. https://doi.org/10.3390/ijms222212596 . PubMed PMID: 34830479; PubMed Central PMCID: PMC8625570.
69. Kitano M, Nakaya M, Nakamura T, Nagata S, Matsuda M. Imaging of Rab5 activity identifies essential regulators for phagosome maturation. Nature. 2008;453(7192):241–5. https://doi.org/10.1038/nature06857 . PubMed PMID: 18385674.
70. Mylvaganam S, Freeman SA, Grinstein S. The cytoskeleton in phagocytosis and macropinocytosis. Curr Biol. 2021;31(10):R619–32. https://doi.org/10.1016/j.cub.2021. 01.036 PubMed PMID: 34033794.
71. Bozzaro S, Bucci C, Steinert M. Phagocytosis and host-pathogen interactions in Dictyostelium with a look at macrophages. Int Rev Cell Mol Biol. 2008;271:253–300. https://doi.org/10.1016/S1937-6448(. 08)01206-9 PubMed PMID: 19081545.
72. Alin AV, Corbett MK, Fathollahzadeh H, Tjiam MC, Putnis A, Eksteen J, et al. Klebsiella aerogenes Adhesion Behaviour during Biofilm Formation on Monazite. Microorganisms. 2023;11(5). https://doi.org/10.3390/microorganisms11051331.
73. Sanders D, Borys KD, Kisa F, Rakowski SA, Lozano M, Filutowicz M. Multiple Dictyostelid Species Destroy Biofilms of Klebsiella oxytoca and Other Gram Negative Species. Protist. 2017;168(3):311–25. https://doi.org/10.1016/j.protis.2017.04.001 . PubMed PMID: 28499132; PubMed Central PMCID: PMC5488719.
74. Ford HZ, Celora GL, Westbrook ER, Dalwadi MP, Walker BJ, Baumann H, et al. Pattern formation along signaling gradients driven by active droplet behavior of cell swarms. Proc Natl Acad Sci. 2025;122(21):e2419152122. https://doi.org/10.1073/pnas.2419152122.
75. Farinholt T, Dinh C, Kuspa A. Social amoebae establish a protective interface with their bacterial associates by lectin agglutination. Sci Adv. 2019;5(7):eaav4367. https://doi.org/10.1126/sciadv.aav4367.
76. Lin Z, Sriskanthadevan S, Huang H, Siu CH, Yang D. Solution structures of the adhesion molecule DdCAD-1 reveal new insights into Ca2+-dependent cell-cell adhesion. Nat Struct Mol Biol. 2006;13(11):1016–22. https://doi.org/10.1038/nsmb1162.
77. Sriskanthadevan S, Zhu Y, Manoharan K, Yang C, Siu CH. The cell adhesion molecule DdCAD-1 regulates morphogenesis through differential spatiotemporal expression in Dictyostelium discoideum. Development. 2011;138(12):2487–97. https://doi.org/10.1242/dev.060129.
78. Ramalingam N, Franke C, Jaschinski E, Winterhoff M, Lu Y, Brühmann S, et al. A resilient formin-derived cortical actin meshwork in the rear drives actomyosin-based motility in 2D confinement. Nat Commun. 2015;6:8496. https://doi.org/10.1038/ncomms9496 . PubMed PMID: 26415699; PubMed Central PMCID: PMC4598863.
79. Šoštar M, Marinović M, Filić V, Pavin N, Weber I. Oscillatory dynamics of Rac1 activity in Dictyostelium discoideum amoebae. PLoS Comput Biol. 2024;20(12):e1012025. https://doi.org/10.1371/journal.pcbi.1012025 . PubMed PMID: 39652619; PubMed Central PMCID: PMC11658709.
80. Kerppola TK. Bimolecular Fluorescence Complementation (BiFC) Analysis as a Probe of Protein Interactions in Living Cells. Annual Rev Biophys. 2008;37:465–87. https://doi.org/10.1146/annurev.biophys.37.032807.125842. 37, 2008.
81. Wong KA, O'Bryan JP. Bimolecular fluorescence complementation. J Vis Exp. 2011;(50):2643. PubMed PMID: 21525844; PubMed Central PMCID: PMC3169261. https://doi.org/10.3791/2643.
82. Miller KE, Kim Y, Huh WK, Park HO. Bimolecular Fluorescence Complementation (BiFC) Analysis: Advances and Recent Applications for Genome-Wide Interaction Studies. J Mol Biol. 2015;427(11):2039–55. https://doi.org/10.1016/j.jmb.2015.03.005 . PubMed PMID: 25772494; PubMed Central PMCID: PMC4417415.
83. Veltman DM, Akar G, Bosgraaf L, Van Haastert PJM. A new set of small, extrachromosomal expression vectors for Dictyostelium discoideum. Plasmid.

2009;61(2):110–8. https://doi.org/10.1016/j.plasmid.2008. 11.003 PubMed PMID: 19063918.
84. Junemann A, Filić V, Winterhoff M, Nordholz B, Litschko C, Schwellenbach H, et al. A Diaphanous-related formin links Ras signaling directly to actin assembly in macropinocytosis and phagocytosis. Proc Natl Acad Sci USA. 2016;113(47):E7464–73. https://doi.org/10.1073/pnas.1611024113 . PubMed PMID: 27821733; PubMed Central PMCID: PMC5127317.
85. Paschke P, Knecht DA, Silale A, Traynor D, Williams TD, Thomason PA, et al. Rapid and efficient genetic engineering of both wild type and axenic strains of Dictyostelium discoideum. PLoS ONE. 2018;13(5):e0196809. https://doi.org/10.1371/journal.pone.0196809 . PubMed PMID: 29847546; PubMed Central PMCID: PMC5976153.
86. Mijanović L, Putar D, Mimica L, Klajn S, Filić V, Weber I. The IQGAP-related RasGAP IqgC regulates cell-substratum adhesion in Dictyostelium discoideum. Cell Mol Biol Lett. 2025;30(1):4. https://doi.org/10.1186/s11658-024-00678-3 . PubMed PMID: 39789437; PubMed Central PMCID: PMC11720917.
87. Dumontier M, Höcht P, Mintert U, Faix J. Rac1 GTPases control filopodia formation, cell motility, endocytosis, cytokinesis and development in Dictyostelium. J Cell Sci. 2000;113(Pt 12):2253–65. PubMed PMID: 10825297.
88. Scholz J, Besir H, Strasser C, Suppmann S. A new method to customize protein expression vectors for fast, efficient and background free parallel cloning. BMC Biotechnol. 2013;13(1):12. https://doi.org/10.1186/1472-6750-13-12.
89. Faix J, Kreppel L, Shaulsky G, Schleicher M, Kimmel AR. A rapid and efficient method to generate multiple gene disruptions in Dictyostelium discoideum using a single selectable marker and the Cre-loxP system. Nucleic Acids Res. 2004;32(19):e143. https://doi.org/10.1093/nar/gnh. 136 PubMed PMID: 15507682; PubMed Central PMCID: PMC528815.
90. Faix J, Linkner J, Nordholz B, Platt JL, Liao XH, Kimmel AR. The application of the Cre-loxP system for generating multiple knock-out and knock-in targeted loci. Methods Mol Biol. 2013;983:249–67. https://doi.org/10.1007/978-1. -62703-302-2_13 PubMed PMID: 23494311.
91. Schindelin J, Arganda-Carreras I, Frise E, Kaynig V, Longair M, Pietzsch T, et al. Fiji: an open-source platform for biological-image analysis. Nat Methods. 2012;9(7):676–82. https://doi.org/10.1038/nmeth.2019.
92. Pfaffl MW. A new mathematical model for relative quantification in real-time RT-PCR. Nucleic Acids Res. 2001;29(9):e45. https://doi.org/10.1093/nar/29.9. .e45 PubMed PMID: 11328886; PubMed Central PMCID: PMC55695.
93. Westphal M, Jungbluth A, Heidecker M, Mühlbauer B, Heizer C, Schwartz JM, et al. Microfilament dynamics during cell movement and chemotaxis monitored using a GFP–actin fusion protein. Curr Biol. 1997;7(3):176–83. https://doi.org/10.1016/S0960-9822. (97)70088-5 PubMed PMID: 9276758.
94. Spudich JA, Watt S. The Regulation of Rabbit Skeletal Muscle Contraction: I. Biochemical studies of the interaction of the tropomyosin-troponin complex with actin and the proteolytic fragments of myosin. J Biol Chem. 1971;246(15):4866–71. https://doi.org/10.1016/S0021-9258(18)62016-2.
95. Inaba H, Yoda K, Adachi H. The F-actin-binding RapGEF GflB is required for efficient macropinocytosis in Dictyostelium. J Cell Sci. 2017;130(18):3158–72. https://doi.org/10.1242/jcs.194126 . PubMed PMID: 28778987.
96. Lin Y, Parajón E, Yuan Q, Ye S, Qin G, Deng Y, et al. Ras-mediated dynamic and biphasic regulation of cell migration. Proc Natl Acad Sci U S A. 2025;122(30):e2503847122. https://doi.org/10.1073/pnas.2503847122 . PubMed PMID: 40694332; PubMed Central PMCID: PMC12318196.
97. Baniukiewicz P, Collier S, Bretschneider T. QuimP: analyzing transmembrane signalling in highly deformable cells. Bioinformatics. 2018;34(15):2695–7. https://doi.org/10.1093/bioinformatics/bty. 169 PubMed PMID: 29566132; PubMed Central PMCID: PMC6061833.
98. Antolović V, Marinović M, Filić V, Weber I. A simple optical configuration for cell tracking by dark-field microscopy. J Microbiol Methods. 2014;104:9–11. https://doi.org/10.1016/j.mimet.2014.06.006 . PubMed PMID: 24950007.
99. Edelstein AD, Tsuchida MA, Amodaj N, Pinkard H, Vale RD, Stuurman N. Advanced methods of microscope control using μManager software. J Biol Methods. 2014;1(2):e10. https://doi.org/10.14440/jbm.2014.36 . PubMed PMID: 25606571; PubMed Central PMCID: PMC4297649.
100. Ershov D, Phan MS, Pylvänäinen JW, Rigaud SU, Le Blanc L, Charles-Orszag A, et al. TrackMate 7: integrating state-of-the-art segmentation algorithms into tracking pipelines. Nat Methods. 2022;19(7):829–32. https://doi.org/10.1038/s41592-022-01507-1 . PubMed PMID: 35654950.
101. Tinevez JY, Perry N, Schindelin J, Hoopes GM, Reynolds GD, Laplantine E, et al. TrackMate: An open and extensible platform for single-particle tracking. Methods. 2017;115:80–90. https://doi.org/10.1016/j.ymeth. 2016.09.016 PubMed PMID: 27713081.
102. Gorelik R, Gautreau A. Quantitative and unbiased analysis of directional persistence in cell migration. Nat Protoc. 2014;9(8):1931–43. https://doi.org/10.1038/nprot.2014.131 . PubMed PMID: 25033209.

Publisher's note

Springer Nature remains neutral with regard to jurisdictional claims in published maps and institutional affiliations.